LEVERAGING CROSS-CORRELATIONS: COSMOLOGY WITH THE KINEMATIC SUNYAEV ZEL'DOVICH EFFECT

A Dissertation

Presented to the Faculty of the Graduate School

of Cornell University

in Partial Fulfillment of the Requirements for the Degree of

Doctor of Philosophy

by

Victoria Rose Calafut

August 2020

LEVERAGING CROSS-CORRELATIONS: COSMOLOGY WITH THE KINEMATIC SUNYAEV ZEL'DOVICH EFFECT

Victoria Rose Calafut, Ph.D.

Cornell University 2020

The current era is one of a wealth of incoming high precision cosmological data from cosmic microwave background (CMB) and large scale structure (LSS) surveys. Yielding precise measurements of the kinematic Sunyaev-Zel'dovich (kSZ) effect, by cross-correlations between the two, has the potential to take advantage of this unique time. In the first chapter of this thesis, we conduct a study on how to achieve this, focusing primarily on systematic effects such as miscentering. Photometric and spectroscopic galaxy tracers from SDSS, WISE, and DECaLs are considered in combination with CMB data from Planck and WMAP. With two complementary techniques, analytic offset modeling and direct comparisons of redMaPPer brightest and central catalog samples, we find that miscentering uncertainties average to $0.4 - 0.7\sigma$ for the Planck kSZ statistical error budget obtained with a jackknife (JK) estimator. Our results demonstrate that uncertainties introduced through using galaxy proxies for cluster locations will need to be fully incorporated, and actively mitigated, for the kSZ to reach its full potential as a cosmological constraining tool for dark energy and neutrino physics. A 5.1σ detection of the pairwise kSZ signal results is obtained with four seasons of ACTPol data in combination with Planck CMB with the luminous red galaxy sample from the Sloan Digital Sky Survey Baryonic Acoustic Oscillation Survey (SDSS BOSS) DR15 catalog, in Chapter 2. We utilize the constraining power of the kSZ effect by fitting each of nine luminosity selected samples to theoretical pairwise predictions, to find kSZ-derived mass-averaged optical depths, τ, and their evolution as a function of cluster mass assum-

ing a Planck cosmology.

BIOGRAPHICAL SKETCH

Victoria Calafut was raised in Manalapan, NJ. From 2010 - 2014, she attended the College of New Jersey, where she majored in Physics with a specialization in astrophysics and self-designed an interdisciplinary concentration in the Philosophy of Science. As an undergraduate, she worked with Dr. Paul Wiita on numerical modeling of relativistic jets in active galactic nuclei. She first worked with Dr. Rachel Bean during a Research Experience for Undergraduates in the summer of 2013, studying primordial non-gaussianity. She continued under the advising of Professor Rachel Bean as a graduate student in the summer of 2014, and obtained an M.Sc. in Astronomy in 2017, before pursuing a Ph.D. in cosomology, with a focus on measurements and analysis of the kinematic Sunyaev Zel'dovich Effect. After completing her Ph.D., she will begin a postdoctoral fellowship at the Canadian Institute for Theoretical Astrophysics in September 2020.

To my parents

ACKNOWLEDGEMENTS

Pursuing a PhD has been a monumental life experience, and without the help of many outstanding people, this work would not have been possible.

I am deeply grateful to my advisor, Professor Rachel Bean, for her unwavering guidance and support. Your mentorship has been invaluable in this experience.

I would like to thank the rest of my special committee, Professors Martha Haynes, Eanna Flanagan, and Michael Niemack for your thoughtful commitment to my graduate success. I would additionally like to thank Professor Nicholas Battaglia as well as Professor Michael Niemack for your feedback and guidance throughout this work. Finally, I would like to extend a thank you to Professor Maxim Perelstein for generously serving as a proxy at my B-exam.

I would also like to express appreciation for the astronomy department at Cornell University and to my fellow graduate students, especially my fellow officemates and "first year" cohort.

Engaging in collaboration-wide science has undoubtedly enriched my graduate career. I would like to thank my colleagues within ACT, SO, DESI, LSST DESC, and Euclid for the experience at meetings, telecons, discussions, and, with ACT, for allowing me to have a unique role in CMB data analysis.

Pursuing my doctorate would not have been possible were it not for my experience at the College of New Jersey. I am thankful to the physics department and to Professor Paul Wiita for his advisement.

Finally I would like to express special gratitude to my family and friends. This would not have been possible were it not for your unconditional support. Thank you to my mom, Arlene, and my dad, Joseph, for being the epitome of this. I am also greatly appreciative of all that my friends have done throughout this journey. Thank you to all!

Victoria Calafut

Ithaca, July 2020

TABLE OF CONTENTS

LIST OF TABLES

LIST OF FIGURES

CHAPTER 1

INTRODUCTION

1.1 The dark energy paradigm

Deciphering the origins of accelerated cosmic expansion [58, 61], encapsulated in the nature of dark energy, is utmost goal in modern cosmology. It is governed by the the scale factor a, used to define the Hubble rate,

$$H(t) \equiv \frac{da/dt}{a}, \tag{1.1}$$

measuring the rate of change of the scale factor. More generally, the evolution of the scale factor is given by the Friedmann equations

$$H^2(a) = \left(\frac{\dot{a}}{a}^2\right) = \frac{8\pi G}{3} - \frac{k}{a^2} \tag{1.2}$$

and

$$\dot{H} + H^2 = \frac{\ddot{a}}{a} = -4\pi G 3(\rho + 3P) = \frac{4\pi G}{3}\rho(1 + 3w), \tag{1.3}$$

where k is the curvature parameter, which is 1,0, or –1 for a closed, flat, or open universe, respectively. Setting this aside, let us look at the Einstein equations of General Relativity (GR)

$$G_{\mu\nu} = R_{\mu\nu} - \frac{1}{2}g_{\mu\nu}R = 8\pi G T_{\mu\nu} \tag{1.4}$$

where $R_{\mu\nu}$ is the Ricci tensor and $R = R_{\mu\nu}g^{\mu\nu}$ is the Ricci scalar. $T_{\mu\nu}$ is the energy-momentum tensor. Here $c = \hbar = 1$. For an isotropic perfect fluid, the energy-momentum tensor can be written as a matrix

$$T^{\mu}_{\nu} = \begin{pmatrix} -\rho & 0 & 0 & 0 \\ 0 & P & 0 & 0 \\ 0 & 0 & P & 0 \\ 0 & 0 & 0 & P \end{pmatrix} \tag{1.5}$$

in which P is pressure and ρ is density. Taking $\nabla_{\mu} T^{\mu\nu} = 0$ yields the continuity equation

$$\dot{\rho} + 3H\rho(1 + w) = 0, \tag{1.6}$$

where the equation of state is given by $w = P/\rho$, which parameterizes the energy density of the universe: a cosmological constant corresponds to $w = -1$, matter to $w = 0$, and radiation to $1/3$.

Dark energy manifests only through its indirect effects: the gravitionally attractive properties of Standard Model particles and dark matter and observed deviations of the laws of gravity from those predicted by GR. Solving 1.5, the Friedmann-Roberston-Walker (FRW) metric describes an expanding homogeneous and isotropic universe without any such modifications:

$$ds^2 = g_{\mu\nu} dx^{\mu} dx^{\nu} = dt^2 + a^2(t) \delta_{ij} dx^i dx^j, \tag{1.7}$$

where δ_{ij} is the Kronecker delta. It is from equations 1.5 and 1.7 that 1.2 and 1.3 are derived.

To determine if dark energy is a cosmological constant, a novel type of matter, or evidence that gravity deviates from GR on cosmic scales, there are three principal cosmological tracers of the gravitational field: the velocities and positions of massive objects and the distortion they create in the geodesic paths of light from more distant objects [58]. We will focus shortly on the utilization on the kinematic Sunyaev-Zel'dovich (kSZ) effect, one of these types of tracers.

1.2 The kSZ effect: cross-correlating CMB and LSS

The Cosmic Microwave Background (CMB) anisotropies are one of the most powerful probes in the early universe. The photons in the CMB last scattered off electrons at redshift 1100 and have since traversed the universe. Collisions with electrons before last scattering yielded the specific intensity of the CMB to be that of a blackbody spectrum:

$$I_\nu = \frac{4\pi\hbar\nu^3/c^2}{\exp(2\pi\hbar\nu/k_BT) - 1}, \tag{1.8}$$

where k_B is the Boltzmann constant, ν is the frequency, and T is the absolute temperature.

Galaxy clusters, each containing hundreds to thousands of galaxies, are the largest gravitationally collapsed cosmological structures [27]. Though the universe appears homogenous and isotropic on large scales, galaxies and galaxy clusters form from initial local matter overdensities and evolve to form the LSS of the universe. According to linear theory the matter overdensity, δ_m, connects the time evolution of perturbations to the dark matter velocity via

$$\dot{\delta}_m \propto v_m. \tag{1.9}$$

The linear perturbation equations have a solution of the form $\delta_m(\vec{x}, t) = D_a(t)\delta(x)$, where D_a is the growth factor. The growth rate at a given scale factor is defined as

$$f_g(a) \equiv \frac{d\ln D_a}{d\ln a}, \tag{1.10}$$

which describes the growth of structure. In terms of the growth index γ,

$$f_g(a) \approx \Omega_m(a)^\gamma, \tag{1.11}$$

where $\gamma \simeq 0.55$ under standard gravity.

Putting the two together, these peculiar motions of galaxy clusters relative to the Cosmic Microwave Background (CMB) rest-frame create Doppler-shift imprints in the

primordial CMB photons as the traverse through the cluster environments and interact with the hot gas they contain. This secondary anisotropy or Doppler shift is known as the kSZ effect. The CMB temperature shift induced by the galaxy cluster's peculiar motion is given by [76],

$$\frac{\delta T_{kSZ}}{T_0}(\hat{r}) = -\int dl\, \sigma_T\, n_e \frac{\mathbf{v}\cdot\hat{\mathbf{r}}}{c}, \tag{1.12}$$

where n_e is the electron number density and σ_T is the Thomson cross-section. A positive peculiar velocity, $\mathbf{v}$, relates to motion away from the observer, so induces a negative kSZ effect.

Concurrently with the kSZ, the CMB photons are also heated up by the cluster gas, the thermal Sunyaev-Zel'dovich effect (tSZ). While the tSZ has a distinctive frequency dependence that can be used to extract it from multi-frequency measurements, the kSZ effect is frequency-independent and approximately twenty times weaker, which make its detection challenging.

The growth of structure is dependent on the underlying theory of gravity. As such, tracers of the underlying dark matter velocity distribution can be used to constrain cosmology and modified gravity models, given the theoretical relationship in equation in 1.7. We will now demonstrate how pairwise kSZ motions represent a probe for cosmological constraints.

Assuming linear theory to describe the mean pairwise streaming velocity, v, between two dark matter particles, in terms of their comoving separation $r = |\vec{r}_i - \vec{r}_j|$, where r_i and r_j are their positions,

$$v(r) = -\frac{2}{3} f_g(a) H(a) a r \frac{\bar{\xi}(r,a)}{1+\xi(r,a)}, \tag{1.13}$$

in which ξ is the dark matter 2-point correlation function and $\bar{\xi}$ is the volume-averaged

correlation function, defined as follows:

$$\xi(r,a) = \frac{1}{2\pi^2}\int dk k^2 j_0(kr)P(k,a), \tag{1.14}$$

$$\bar{\xi}(r,a) = \frac{3}{r^3}\int_0^{r^3} dr'\xi(r,a), \tag{1.15}$$

where P(k, a) is the dark matter power spectrum and $j_0 = sin(x)/x$ is the $0th$ order Bessel function.

On scales of the order of ∼100 Mpcs, the gravitational attraction between clusters of galaxies causes them to move inward towards each other on average. As such, a pairwise statistic is utilized to extract the kSZ effect and is a useful approach because of its dependence on linear differences of measured temperatures on the sky at the positions of clusters, averaging out contaminating signals like the tSZ signal and dust emission. The pairwise kSZ momentum is shown to have the potential to probe the LSS growth rate (equations 1.7 and 1.8), being sensitive to both the cluster peculiar velocity and optical depth as in equation 1.9. This provides insights to the evolution of dark energy, cosmic modifications to gravity over cosmic time, and constraints on the sum of the neutrino masses [16, 54, 53, 26].

1.3 Measuring the kSZ effect

As discussed, to obtain pairwise kSZ measurements, an overlapping CMB map and galaxy survey are required. Typically, luminous red galaxies (LRGs) are used to represent the galaxy cluster center, the location of the temperature distortion of the CMB photons photons due to the motion of cluster's ionized gas. It is thought that LRGs trace cluster centers, and the most massive are Bright Halo Galaxies (BHG), since the central galaxy in the dark matter halo is the most massive and luminous galaxy due to contin-

ued gas accretion. The Sloan Digital Sky Survey (SDSS) [29] is a spectroscopic survey, while the Dark Energy Survey [72] and Wide-field Infrared Survey Explorer (WISE) measure photometric data and as such induce photometric redshift uncertainities. Unlike other methods, the pairwise estimator is sensitive to redshift.

When cross-correlating with CMB maps, the relative resolution compared to the characteristic size of a galaxy cluster is significant. Assuming a cluster of size 1 Mpc, for galaxies at redshifts comparable to those in SDSS-BOSS, the angular-diameter distance corresponds to around 2 arcmin. For comparison, the Planck collaboration has made 5, 8, and 12 arcmin CMB measurements [5], while the newest combined ACTPol-Planck maps have reached 0.5 arcminute resolution.

Looking forward, there are several current and upcoming surveys and next generation CMB science experiments with which kSZ science can be done. With multi-frequency data and increased detection area, there is potential for the increased SNR measurements. Such instruments include Simon's Observatory (SO), CMB-S4, CCAT, Euclid, and the Dark Energy Spectroscopic Instrument (DESI).

1.4 Overview

In Chapter 2, this miscentering problem is discussed and analyzed in-depth, utilizing Planck CMB maps. In Chapter 3, a 5.1σ pairwise kSZ signal is detected using ACTPol and ACT+Planck CMB maps. A study of systemics or analysis assumptions, respectively, is undertaken in each. Our measurements are fit to theory predictions to obtain optical depth estimates (in Chapter 3). Our conclusions are drawn together in Chapter 4. The analysis assumptions discussed in Chapter 3 are laid out in detail in Appendix A.

CHAPTER 2

CLUSTER MISLOCATION IN KINEMATIC SUNYAEV ZEL'DOVICH (KSZ) EFFECT EXTRACTION

2.1 Introduction

The last decade has seen large scale primordial Cosmic Microwave Background (CMB) temperature and polarization anisotropies measured down to cosmic variance levels, with the Wilkinson Microwave Anisotropy Probe (WMAP) [36], and Planck [59] satellites. Concurrently, the measurement of anisotropies at arcminute scales, for example with Planck [5], the Atacama Cosmology Telescope (ACT) [20], and South Pole Telescope (SPT) [70], has led to first detections of secondary anisotropies, those imprinted in the CMB, following recombination, as the photons traverse large scale structures. This includes the measurement of the thermal and kinetic Sunyaev-Zel'dovich effects (tSZ and kSZ, respectively) [75] and gravitational lensing of the CMB [35]. This work has been published as [17].

Marked improvements in sensitivity, and an expansion of frequencies surveyed, at arcminute scales will be available with upgrades to the ACT and SPT facilities, Advanced ACTPol [56] and SPT-3G [1], and the construction of new facilities, including the Simons Observatory [2], the CCAT-prime observatory [3] and a next generation 'Stage-4' ground-based CMB experiment, "CMB-S4" [2]. These promise a wealth of secondary anisotropy data that could provide rich and mutually complementary information about the properties and evolution of galaxies and galaxy clusters, based on tracers of the ionized gas and gravitational potential.

[1] https://pole.uchicago.edu
[2] http://simonsobservatory.org/
[3] https://www.ccatobservatory.org/

This chapter focuses on the impact of extraction and analysis assumptions on kSZ signal and covariance estimation. The kSZ effect is a Doppler distortion in the CMB produced by the bulk motion of the cluster with respect to the CMB rest frame. Accurate measurements of the kSZ might therefore allow the inference of peculiar motions of the most massive structures in the universe, and provide a powerful probe of the large scale structure (LSS) of the universe. The LSS growth rate can provide insights to central questions in cosmology, including the evolution of dark energy and cosmic modifications to gravity over cosmic time, and constraints on the sum of the neutrino masses [16, 53, 54, 26].

While the tSZ has a distinctive frequency dependence that can be used to extract it from multi-frequency measurements, the kSZ effect is frequency-independent and approximately twenty times weaker. A variety of techniques are being developed to extract the kSZ at cluster locations obtained from external LSS survey catalogs at other frequencies. Cluster bulk flows have been estimated with the kSZ effect [28, 41, 44] using WMAP and Planck data and X-ray detected clusters [43, 42, 57, 52, 60]. Combined kSZ and tSZ measurements of individual clusters have yielded constraints on their peculiar velocities [37, 12].

A number of recent surveys have demonstrated the potential for extracting the pairwise kSZ signal from CMB data in combination with galaxy surveys to locate the clusters [43, 41, 25, 46, 74]. The first statistically significant kSZ detection was achieved using the pairwise estimator with ACT CMB data [30] in tandem with spectroscopic luminous red galaxies (LRGs) from the Baryon Oscillation Spectroscopic Survey (BOSS) survey [7]. This has been extended upon with kSZ measurements from SPT [72] in combination with photometric galaxy survey information from the Dark Energy Survey (DES) [65], with Planck [5] in combination with the Sloan Digital Sky Survey (SDSS)

Central Galaxy Catalog (CGC) [1] and from ACTPol with BOSS [69, 23]. New techniques beyond the pairwise statistic have recently been developed to measure the kSZ signal, including new matched-filter estimators [48] and three-point statistics [34, 24].

Galaxies are often used as proxies to identify and locate the centers of galaxy clusters for kSZ extraction. A typical assumption is that the brightest halo galaxy (BHG) pinpoints the center of the cluster region where the temperature of the CMB photons is altered due to the motion of cluster's ionized gas. This approach follows the 'Central Galaxy Paradigm' [77] in which the central galaxy in the dark matter halo is the most massive and luminous galaxy due to continued gas accretion, relative to tidal stripping and ram-pressure quenching of star formation in captured satellite galaxies. In observations, miscentering biases can arise from the misindentification of the cluster central galaxy. In spectroscopically selected galaxy catalogs, luminosity and color cuts are used to isolate the brightest, red galaxies. Photometrically selected catalogs can typically include many cluster members, or potential members, not just the single brightest, and have been used to determine how well BHGs trace the cluster center.

In simulations the cluster central galaxy is defined as the location of the gravitational potential minimum, coinciding with the projected center of the electron distribution for kSZ extraction. Using the Red-sequence Matched-filter Probabilistic Percolation (redMaPPer) [63] algorithm studies have found ~20% [39] to ~40% [71] of the BHGs are off-centered when considering ranked centering and cluster membership probabilities. As a result there can be detriments to the kSZ signal due to the fact that even the true BHG does not always trace the location of the potential minimum [26]. RedMaPPer has also provided evidence of anti-correlations between central galaxy brightness and cluster mass at fixed richness that could signal cluster mergers that might result in galaxy position disruption that would effect the applicability of the central galaxy

paradigm [39]. A variety of analytical offset models, based on observations, are also used to model and quantify the impact of miscentering for BHG data; they typically assume a fraction of galaxies have a Gaussian, or double Gaussian, miscentering distribution [40, 68]. Previous miscentering work has been done applying analytical offset models with simulations, finding a biased amplitude averaged over separation bins up to 200 Mpc as large as 11% [26].

In addition to transverse mis-identification of cluster positions, photometric redshift errors induce radial uncertainties in cluster locations that can also dilute statistical power in the pairwise estimator [45, 72].

In this chapter we characterize the size and nature of the impact of a variety of analysis assumptions for the extraction of the pairwise kSZ signal and covariance estimation for current CMB and LSS datasets. We consider different covariance estimation techniques, assumptions in kSZ decrement estimation, and the impact of both transverse miscentering and photometric redshift ('photo-z') errors. We utilize data from Planck and WMAP CMB surveys, and SDSS, WISE, and DECaLs LSS surveys. Understanding the impact of these assumptions on current surveys is an important practical step in order to assess the implications of the kSZ science potential of future spectroscopic and photometric surveys, including DESI, LSST and Euclid, and complements work in tandem on simulated datasets [45, 26].

Our work is organized as follows: in section 3.2, the CMB datasets and large scale structure surveys used in the analysis are described. The analytical formalisms used for: the pairwise estimator and background on signal extraction; covariance estimation; and miscentering models, are outlined in section 3.3. Our results are discussed in section 3.4, and the findings and their implications for future work are drawn together in section 3.5.

2.2 Datasets

In order to extract the kSZ signal temperatures, we cross-correlate CMB maps and galaxy survey catalogs, from which the locations of the brightest central galaxies are, as the default, assumed to trace the cluster centers. In this section we describe the different CMB and galaxy survey data sets used in the analysis.

2.2.1 CMB maps

In this analysis we use the publicly available, foreground-cleaned *Planck* SEVEM (Spectral Estimation Via Expectation Maximization) map [3][4]. The NSIDE = 2048 HEALPix [5] SEVEM map covers, after confidence masks and foreground subtraction, approximately 85% of the full sky temperature map and a 5 arcmin FWHM [5]. We have also conducted comparable analyses with the the foreground-, dust-, and tSZ-cleaned LGMCA ("local-generalized morphological component analysis") map [15][6], derived from a joint analysis of WMAP and Planck and find the results are nearly identical, with no significant differences induced for the aperture photometry as result of the different foreground removal approaches, including for tSZ removal, used to produce the maps.

2.2.2 Galaxy samples

Two methods with galaxy surveys are used to identify clusters and their center location to extract the kSZ from the CMB samples.

[4] http://pla.esac.esa.int/pla/
[5] http://healpix.sourceforge.net
[6] http://www.cosmostat.org/product/ LGMCA_cmb

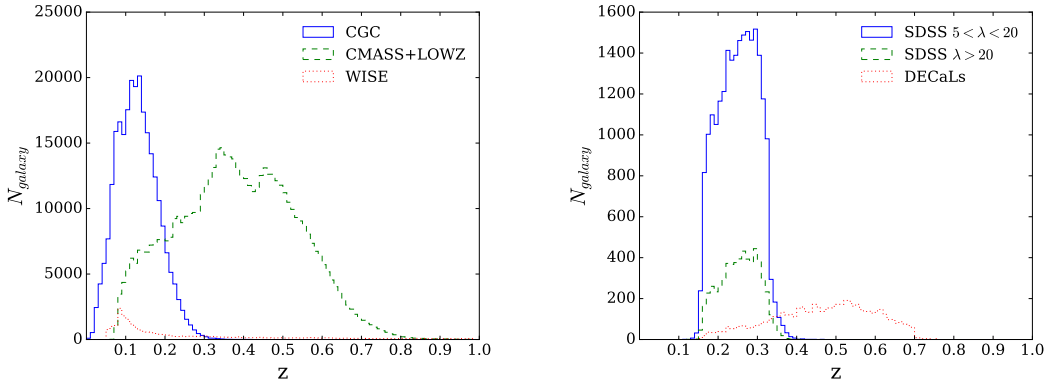

Figure 2.1: [Left] The galaxy number distributions as a function of redshift, z, for the spectroscopic-selected galaxy samples, showing SDSS CGC [full line], CMASS+LOWZ [dashed line] and WISE [dotted line] samples. [Right] The redshift distributions for the redMaPPer catalogs: two SDSS redMaPPer samples with low [full] and high [dashed] richness, λ, and a sample from DECaLs [dotted]. Further details about the samples are given in Table 2.1.

The first approach uses spectroscopic LSS data, which gives precise redshifts for a select sample of bright, red galaxies, to identify and locate each cluster by targeting the brightest central galaxy following the Central Galaxy Paradigm. One option is to impose an aggressive luminosity cut, to include only the very brightest in the sample for cross-correlation. This avoids multiple galaxies being included in each cluster but also has the risk of not identifying all clusters, by excluding some of the less luminous brightest central galaxies. An alternative is a less aggressive luminosity cut, combined with the exclusion, around each bright galaxy, of other fainter galaxies within a characteristic cluster radius from the sample. This will lead to a more complete identification of cluster but, if the luminosity threshold is too low, could lead to satellites being mis-identified as the cluster center.

Three primarily spectroscopically selected "Brightest Galaxy" catalogs and three primarily photometrically selected redMaPPer galaxy samples are considered in this work. Their redshift distributions are shown given in Figure 2.1, and the selection crite-

ria, redshift information and total catalog size for each sample are described below.

Brightest Galaxy Catalog datasets

For the first of our brightest galaxy catalogs, the SDSS Central Galaxy Catalog (CGC), we utilize the catalog from [5][7]. This contains 262, 671 sources, selected based on the isolation criterion such that each galaxy is the brightest extinction-corrected r-band galaxy with $r < 17.7$ found within 1.0 Mpc transverse distance and redshift difference corresponding to 1000 km s^{-1}. It includes an additional cut to account for potential companions which fail to have a spectroscopic redshift due to fiber collision; this is done by cross-comparing using the photometric "redshift-2" catalog [18], available at [8].

The luminosity range is $-29.8 < R < -11.9$. Recent work in the ACT collaboration used a more aggressive luminosity cut corresponding to approximately $R < -22.8$ for their BOSS galaxy sample sample [9]. To compare the impact of such variations in the luminosity cutoff, we also consider a stricter CGC sample with absolute R-band Petrosian magnitude, $R < -20.5$, corresponding to the mean value for the sample, compared to the initial $R < -11.9$, retaining 140, 933 galaxies of the original 262, 671.

We create a WISE cluster-center catalog based on the color criterion used for the galaxy sample in [33] comprised of 10^6 galaxies with $r < 17.7$ obtained from the WISE All-Sky Data Release Catalog [79]. Selection conditions are then applied: isolating the brightest extinction-corrected red galaxy within bins of roughly 12 by 12 arcmin across the sample, further removing any galaxies which are not the brightest in 1 Mpc transverse and radial separations, and cross-matching using the WISEx_match function

[7] Wenting Wang & Carlos Hernández-Monteagudo, private communication
[8] http://das.sdss.org/va/photoz2/
[9] http://data.sdss3.org/sas/dr11/boss/lss/

[10], in the SDSS DR12 CasJobs query database to obtain redshifts, retaining 63,085. Two additional cuts are made based on redshift: galaxies with $z < 0.05$ are removed as we find the aperture photometry method presents at redshifts below this threshold require unreasonably large apertures sizes to trace the kSZ signal. Roughly 90% of the original sample redshifts are photometric, we exclude approximately 20,000 low redshift galaxies with $\sigma_{phot}/z > 0.1$ to exclude those with poor photo-z estimates; this reduces the final sample size to 24,731.

We consider a combined CMASS and LOWZ sample from the public DR11 Large Scale Structure catalog [11] from the SDSS-III Baryon Oscillation Spectroscopic Survey (BOSS) [22]. To the combined base catalog, exceeding one million galaxies, we apply a magnitude criteria corresponding to galaxies with absolute R-band Petrosian magnitudes brighter than -21.4 in order to maintain a sufficiently selective sample of bright galaxies, giving a sample of 555,307. The choice of $R < -21.4$ corresponds to the mean value for the full selection of galaxies in the initial catalog.

redMaPPer datasets

In addition to the principally spectroscopic BCG catalogs described above, we consider three catalogs created using the redMaPPer algorithm, which include a higher fraction of photometric redshifts [64]. These allow us to simultaneously study the relative impacts of photometric redshift and transverse miscentering uncertainties related to using the BHG to pinpoint the cluster center.

The photometric redMaPPer (RM) data identifies and locates galaxy clusters using iterative red-sequence modeling, based on the fact that old, red galaxies make up the

[10] https://skyserver.sdss.org/dr12/
[11] http://data.sdss3.org/sas/dr11/boss/lss/

bulk of clusters and that the brightest, most massive galaxies reside in the cluster center. With the redMaPPer algorithm, a membership probability $P_{mem,ij}$ is assigned to the i^{th} galaxy associated with the j^{th} cluster and also assigned a rank in centering probability in that cluster, $P_{cen,ij}$ [65].

We consider cluster catalogs selected based on their "richness", λ, a reasonable measure of cluster mass for photometric surveys [62]. This is determined by sum of the membership probabilities, for all N_{gal} galaxies associated with the cluster,

$$\lambda_j = \sum_{i=1}^{N_{gal}} P_{free,i} P_{mem,ij}, \tag{2.1}$$

where P_{free}, typically ≈ 1, is the probability that a galaxy within the cluster is not a member of another cluster within a characteristic, richness dependent cutoff radius,

$$R_c(\lambda) = R_0 \left(\frac{\lambda}{100}\right)^{\beta}, \tag{2.2}$$

with $R_0 = 1.0\text{Mpc}/h$ and $\beta = 0.2$ [66]. We use the redMaPPer central galaxy (RMCG) catalog from the SDSS DR8 cluster catalog (v5.10) [67] and the DECaLs DR2 catalog v6.4.12 [62, 65]. The central galaxy is found by selecting the galaxy within each cluster with the highest centering probability as computed with the redMaPPer cluster-finding algorithm [64]. The SDSS RMCG high-richness catalog, with $\lambda > 20$, includes $7,730$ SDSS DR8 clusters (of which 5,818 center-proxy galaxies meet the criteria to be an LRG) and $507,874$ total member galaxies spanning $0.16 < z < 0.33$. Brightness is restricted to $i < 21.0$. We also analyze a subset over the same redshift range for which $5 < \lambda < 20$ for which there are $22,492$ cluster-center proxy LRGs and $1,878,746$ total member galaxies [38], [65]. However, we recognize that this dataset is not as reliable as high richness sample, due to the lower number of member galaxies and the lower likelihood of those galaxies being associated with clusters.

The final catalog we consider is not publicly available [12], but is a preliminary

[12] Eduardo Rozo & Eli Rykoff, private communication

redMaPPer central galaxy catalog of the Dark Energy Camera Legacy Survey (DECaLs) DR2 RMCG that overlaps with the CMASS+LOWZ sample. The higher redshift DECaLs RMCG contains $5,870$ most likely cluster-center proxies, out of 30,020 total member galaxies, of which 43% have photometric redshifts only. All have $\sigma_z/z < 0.1$, eliminating the need apply this criteria as we did for WISE.

2.3 Formalism

2.3.1 Pairwise estimator

The temperature distortion in the CMB induced by the cluster's peculiar motion is given by [76],

$$\frac{\delta T_{kSZ}}{T_0}(\hat{r}) = -\int dl\, \sigma_T\, n_e \frac{\mathbf{v}\cdot\hat{\mathbf{r}}}{c} \tag{2.3}$$

where n_e is the electron number density and σ_T is the Thomson cross-section. A positive peculiar velocity, $\mathbf{v}$, relates to motion away from the observer, so induces a negative kSZ effect. For the case in which the kSZ signal is dominated by a single cluster along the line of sight

$$\frac{\delta T_{kSZ}}{T_0}(\hat{r}) = -\tau\frac{v_r}{c} \tag{2.4}$$

where τ is the cluster optical depth and v_r is cluster line of sight peculiar velocity. The kSZ effect itself is a direct measure of the cluster momentum, since it is dependent on both the velocity of the cluster and the number density of electrons. As a measure of their gravitational infall, clusters are likely to be moving towards each other, and this should show up in the correlation of cluster velocities, and hence in the related kSZ signature in the CMB. To obtain the peculiar velocity correlations traced by the kSZ

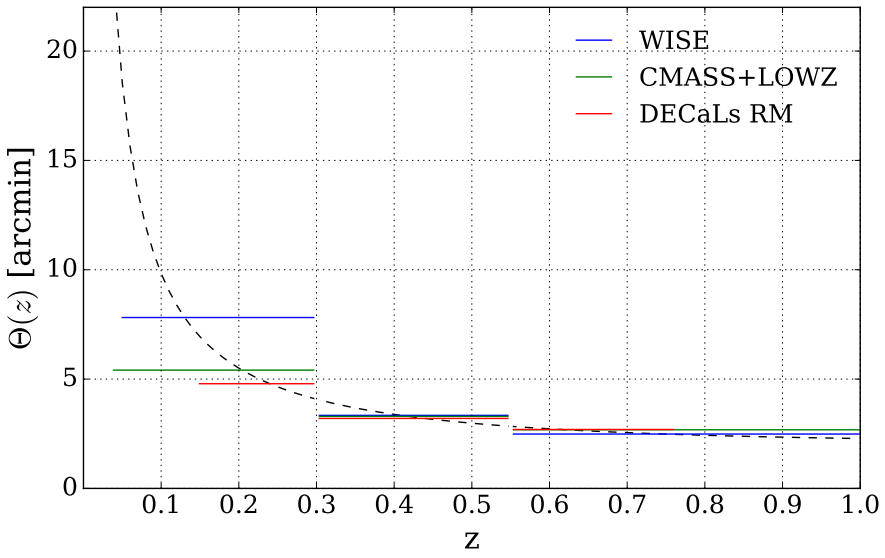

Figure 2.2: The redshift-dependent aperture used for the aperture photometry kSZ temperature decrement estimation for the WISE [blue] and CMASS+LOWZ [green] samples and DECaLs redMaPPer (RM) catalog [red], which have galaxies distributed over extended redshift ranges. The angular size of a 1.1 Mpc galaxy cluster as a function of the redshift is shown for comparison [dotted line].

effect, we employ the pairwise estimator, derived by Ferreira et al. [25]. The pairwise momentum estimator is given by [30],

$$\hat{p}_{kSZ}(r) = -\frac{\sum_{i<j}(\delta T_i - \delta T_j)c_{ij}}{\sum_{i<j} c_{ij}^2}, \tag{2.5}$$

where the sum is over all galaxy cluster pairs, located at positions $\mathbf{r}_i = \{\hat{\mathbf{r}}_i, z_i\}$ and $\mathbf{r}_j = \{\hat{\mathbf{r}}_j, z_j\}$, separated by a distance $r = |\mathbf{r}_{ij}| = |\mathbf{r}_i - \mathbf{r}_j|$, and with $\hat{\mathbf{r}}$ the unit vector in the direction of $\mathbf{r}$. δT_i represents the relative kSZ temperature at the i^{th} cluster location. The weights c_{ij} are given by

$$c_{ij} = \hat{r}_{ij} \cdot \frac{\hat{r}_i + \hat{r}_j}{2} = \frac{(r_i - r_j)(1 + cos\alpha)}{2\sqrt{r_i^2 + r_j^2 - 2r_i r_j cos\alpha}} \tag{2.6}$$

where α is the angle between $\hat{r}_i$ and $\hat{r}_j$.

2.3.2 Signal extraction

We employ aperture photometry (AP) to isolate the kSZ signal from the CMB. This technique relies upon the kSZ being localized in the cluster, while the primordial CMB modes, correlated over longer wavelengths, are removed by differencing the cluster region with an annular region immediately adjacent to it. The aperture photometry temperature, $T_{AP} = \langle T_{inner} \rangle - \langle T_{annul} \rangle$, is the difference between the average CMB pixel temperature within a given angular radius Θ, comparable to the cluster size, to that within an annulus, outside the radius, of width $\sqrt{2}\Theta$. A cluster of scale 1.1 Mpc is used as the basis for the typical angular size for the aperture.

As summarized in Figure 2.1, our analyses include some galaxy samples that are relatively compact in redshift space, SDSS CGC, and the SDSS redMaPPer datasets, and others that have broader redshift distributions, WISE and CMASS+LOWZ. To accommodate these differences, we compare pairwise results using two alternative aperture size criteria. For all datasets, we consider a single, redshift-independent aperture, fixed by the typical cluster angular size, $\Theta(\bar{z})$ at the survey's mean redshift, $\bar{z}$. For the datasets that are extended in redshift, a redshift-dependent aperture, $\Theta(z)$, which is binned for the clusters in each sample in three ranges, $z < 0.3$, $0.3 < z < 0.55$, and $z > 0.55$ is also considered. The values of the redshift-dependent aperture are shown in Figure 2.2 and the single aperture values for each sample summarized in Table 2.1.

The cluster kSZ decrement is then given by

$$\delta T_i(\hat{r}_i, z_i, \sigma_z, \Theta) = T_{AP}(\hat{r}_i, \Theta) - \bar{T}_{AP}(\hat{r}_i, z_i, \sigma_z, \Theta). \tag{2.7}$$

where $T_{AP}(\hat{r}_i, \Theta)$ corresponds to the kSZ amplitude estimate obtained at the angular position of the i^{th} galaxy with an aperture size Θ, and $\bar{T}_{AP}$ is the averaged aperture temperature over all cluster locations within a Gaussian distributed redshift range centered

Brightest Galaxy Catalogs:

Sample	N_{gal}	$\bar{z}$	σ_z	$\Theta(\bar{z})$
SDSS CGC	262,671	0.13	0.05	8.0'
WISE	24,731	0.27	0.24	4.8'
CMASS+LOWZ	555,307	0.46	0.15	3.2'

redMaPPer-derived Catalogs:

Sample	N_{gal}	$\bar{z}$	σ_z	$\Theta(\bar{z})$
SDSS ($5 < \lambda < 20$)	22,492	0.25	0.05	4.7'
SDSS ($\lambda > 20$)	5,818	0.26	0.05	4.6'
DECaLs	5,870	0.47	0.13	3.1'

Table 2.1: Overview of the galaxy samples considered in the analysis: [upper] three spectroscopically selected brightest galaxy samples and [lower] three primarily photometric redMaPPer Central Galaxy Catalogs (RMCG), for which the SDSS samples are delineated on the basis of richness, λ. For each sample, the number of galaxies in the same, N_{gal}, their mean redshift, $\bar{z}$, and standard deviation, σ_z, and the aperture size of a 1 Mpc scale at $\bar{z}$, $\Theta(\bar{z})$, is given.

on the cluster, z_i, with width σ_z, introduced by [30] to account for possible redshift evolution of the tSZ signal in the sources:

$$\bar{T}_{AP}(\hat{r}_i, z_i, \sigma_z, \Theta) = \frac{\sum_j T_{AP}(\hat{r}_i, \Theta) \exp\left(-\frac{(z_i - z_j)^2}{2\sigma_z^2}\right)}{\sum_j \exp\left(-\frac{(z_i - z_j)^2}{2\sigma_z^2}\right)}. \tag{2.8}$$

The sum is over all galaxies $j \neq i$ in the same redshift bin, and we take $\sigma_z = 0.01$ as in previous work by the Planck team [5].

2.3.3 Covariance estimation

We compare covariance estimates using two distinct methods that have been used in pairwise kSZ studies in the literature: CMB map rotations and jackknife (JK) resam-

pling.

For the angular rotation method, as in [5], we produce 50 sets of angular rotations relative to the real cluster-center positions, using a displacement step of three times the aperture radius adopted, and have confirmed that there is very little deviation in the variance with the number of rotations performed. The assumption is that the displaced samples reflect a set of null realizations.

For the JK covariance estimate, we create resamples of the pairwise kSZ measurement by binning the clusters into N_{JK} subsamples, removing one, and then computing the pairwise estimator according to the remaining $(N_{JK} - 1)$ subsamples. This is done such that each subsample is removed precisely once. The covariance matrix is then given by

$$\hat{C}_{ij}^{JK} = \frac{N_{JK} - 1}{N_{JK}} \sum_{\beta=1}^{N_{JK}} (\hat{p}_i^\beta - \bar{p}_i)(\hat{p}_j^\beta - \bar{p}_j), \tag{2.9}$$

where $\hat{p}_i^\beta$ is the pairwise kSZ signal in separation bin i and JK subsample β, with mean of the N_{JK} samples, $\bar{p}_i$ [73]. We use $N_{JK} = 100$ submaps for all analyses and find that covariance estimates are largely insensitive to changes around this subsample size (we considered $N_{JK} = 50, 100, 250$). We also confirmed that the results were unaffected by limiting to longitudinal rotations only, as in [5], versus including both longitudinal and latitudinal as we use in modeling the miscentering offset.

2.3.4 Cluster centering estimation

The effectiveness of the aperture photometry technique is dependent on the ability to identify and locate the center of each galaxy cluster. As discussed in the introduction, astrophysical processes including cluster merges can introduce systematic offsets in the locations of the brightest, most massive galaxies, typically expected to exist in the clus-

ter's central region [50].

We consider two approaches to study the effect of cluster miscentering on the kSZ signal: 1) contrasting redMaPPer selected catalogs of the brightest versus the most likely central galaxies, 2) using an analytic Johnston model (based on photometric catalog analyses) [40].

We directly test Central Galaxy Paradigm with the redMaPPer data by considering the differences in the predicted signal if the "cluster center" is assigned to RM-identified galaxies, other than the one with highest probability central galaxy. Following the approach discussed in [39], we create two catalogs from the RM data, for each of two populations, $5 > \lambda > 20$ and $\lambda < 20$: a redMaPPer central galaxy (RMCG) catalog, based on the highest rank cluster center, and the redMaPPer brightest galaxy (RMBG) catalog. For the brightest galaxy catalogs, we then consider an analytical offset model by Johnston et al. [40], obtained through comparing weak lensing profiles with brightest galaxy positions in the SDSS galaxy clusters. It assumes that a fraction of the cluster sample, f_J, has precisely known centers, corresponding to where the brightest galaxy is close to the cluster's gravitational potential minimum, and the remaining $(1 - f_J)$ have a brightest galaxy a distance d from the center, with a probability following a Rayleigh distribution function of width σ_J:

$$p_J(d) = \frac{d}{\sigma_J^2} \exp\left(-\frac{d^2}{2\sigma_J^2}\right). \tag{2.10}$$

Johnston et al. find a reasonable fit to their BHGs with σ_J=0.42 Mpc/h, and find a richness dependent fraction of BHGs are well-centered, ranging from $f_J \sim 60{-}90\%$ for clusters of mass $5 \times 10^{12} - 5 \times 10^{14} M_{sun}/h$ respectively.

We estimate the fraction of clusters for which the brightest target galaxy is at the cluster center and the offset size for those that are miscentered, f_J and σ_J, by using the redMaPPer samples, summing over the probabilities of scenarios in which the galaxy

with the highest centering probabilities may in fact not be a true member of the cluster, presented here in a slightly modified form from the centering probability in [38]:

$$N \cdot f_J \approx \sum_{i=1BG} P_{cen,i}(P_{mem}^{1BG}) + \sum_{i=2BG} P_{cen,i}(1 - P_{mem}^{1BG}) + \sum_{i=3BG} P_{cen,i}(P_{mem}^{1BG})(1 - P_{mem}^{2BG}) + \sum_{i=4BG} P_{cen,i}(P_{mem}^{1BG})(1 - P_{mem}^{2BG})(1 - P_{mem}^{3BG}) + ... \quad (2.11)$$

where N is the number of clusters. For each central candidate target (e.g. LRG) galaxy i, we calculate $P_{cen,i}$ weighted by the probability that it is the brightest member galaxy as well. Here nBG refers to the nth brightest target galaxy in the cluster. For example, when the brightest galaxy (1BG) in the cluster is also the central candidate galaxy, f_J is found by summing the centering probabilities with just the first term. The centering probabilities are normalized such that $\sum_i P_{cen,ij}$=1. We consider the first five BG terms only because the probability that none of the first five brightest galaxies are cluster members is negligible.

2.4 Analysis

2.4.1 Covariance method comparison

As described in section 3.3.2, the JK method involves splitting the dataset into some number N_{JK} submaps and finding the variance based on computing the signal with each submap removed exactly once. The rotation method estimates the covariance using the variance between the pairwise signals obtained after random longitudinal displacements of cluster locations by three times the aperture size.

In Figure 2.3, we show the results using the two covariance methods for our datasets

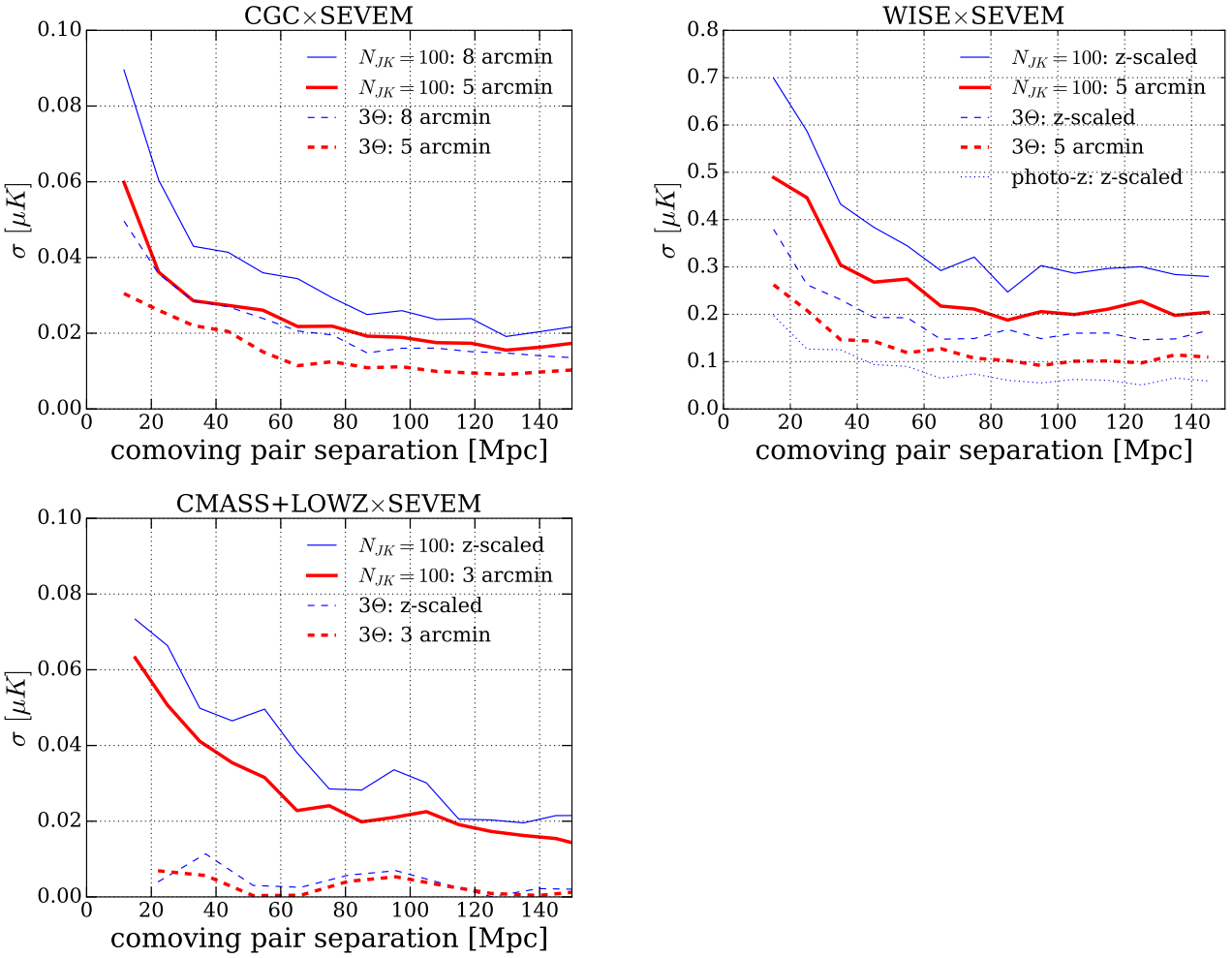

Figure 2.3: Comparison of the standard deviation, σ, in $\hat{p}_{kSZ}$ for the *Planck* SEVEM dataset as a function of comoving pair separation when cross-correlated with the SDSS CGC [left], WISE [center], and CMASS+LOWZ [right] galaxy samples using different covariance estimation techniques. In each plot, the errors estimated from a jackknife (JK) resampling, using $N_{JK} = 100$ subsamples [full lines], are compared with those from maps with 50 randomly oriented rotations of displacements of 3×the aperture size, denoted by "3Θ" [dashed lines]. The CGC×SEVEM rotation errors with 5 [red, thick] and 8 [blue, thin] arcmin apertures, are consistent with those presented by the Planck collaboration [5]. The WISE and CMASS+LOWZ results compare statistical errors for fixed apertures [red, thick] with redshift dependent ('z-scaled') apertures [blue, thin].

with the *Planck* SEVEM maps. We find that the JK method predicts larger covariances than the rotation method for the same aperture at all pairwise separations considered ($15 - 150$ Mpc).

The covariance for both techniques is found to be sensitive to the aperture size. At an intermediate separation of 55 Mpc, cross-correlations with the CGC catalog, the JK method estimates a standard error, σ, that is 1.7 larger than that predicted for rotations for an 8 arcminute aperture. For a smaller aperture size, that likely slightly underestimates the cluster size, the variance estimate is also smaller for both methods consistent with some of the signal being removed in the aperture photometry differencing. The WISE sample shows similar findings in comparing the two methods, with a factor of 2.3 difference in variance between the JK and rotation methods. It also shows that the aperture size choice when choosing either a fixed aperture at an average value or varying with redshift can affect the covariance estimate for samples which are extended in redshift space. We find a large disparity between the two methods for CMASS+LOWZ×SEVEM, the cross-correlation with the most galaxies, with factors of ~ 8 between the JKs and rotations for both the redshift dependent and fixed apertures.

Given the JK errors are more conservative than those from the rotations, and that the JK method is found to be reliable compared to estimates from simulations [23], we use these errors for the analysis in the remainder of the chapter.

2.4.2 $\hat{p}_{kSZ}$ sensitivity to galaxy sample, CMB map creation, and aperture choice

In this section we consider the impact on the pairwise estimator of assumptions that go into: the galaxy proxy sample selection; the CMB map generation; and the aperture photometry method.

In the left panel of Figure 2.4, we compare pairwise correlations for the CGC sample using Planck CMB maps with the same aperture photometry but in which the CMB pixels are noise weighted while in the other a flat-weighting is used. We find little difference, with only a marginal improvement in the $\hat{p}_{kSZ}$ aperture photometry results by down-weighting the noisy pixels in the map. Based on this we use a flat weighting in the remainder of the analyses.

In section 3.2.2, we describe the criteria used to develop the galaxy samples used as proxies to identify and locate clusters. These assumptions can be highly varied across the analyses in the literature. The right panel of Figure 2.4, demonstrates the impact of the luminosity cut assumptions in the galaxy proxy catalog. p_{kSZ} is shown for the SEVEM map when cross-correlated with the CGC catalog from the Planck analysis [5] an apparent r-band magnitude cut was imposed, and with the redshift distribution of the sample, this translates into a redshift dependent absolute magnitude cut of $-29.8 < R < -11.9$, comprising $262,671$ galaxies. We also show results for a catalog with a stricter luminosity cut, $R < -20.5$, with $140,933$ galaxies. These magnitude cuts respectively correspond to luminosity thresholds of $\sim 3.5 \times 10^6 L_{sun}$ and $\sim 8.8 \times 10^8 L_{sun}$. By comparison, recent work by the ACT collaboration considered a luminosity cut of $L > 7.9 \times 10^{10} L_{sun}$ [23]. The more conservative threshold was chosen so as to maintain at least 100,000 galaxies in the sample most likely to represent a central galaxy sample,

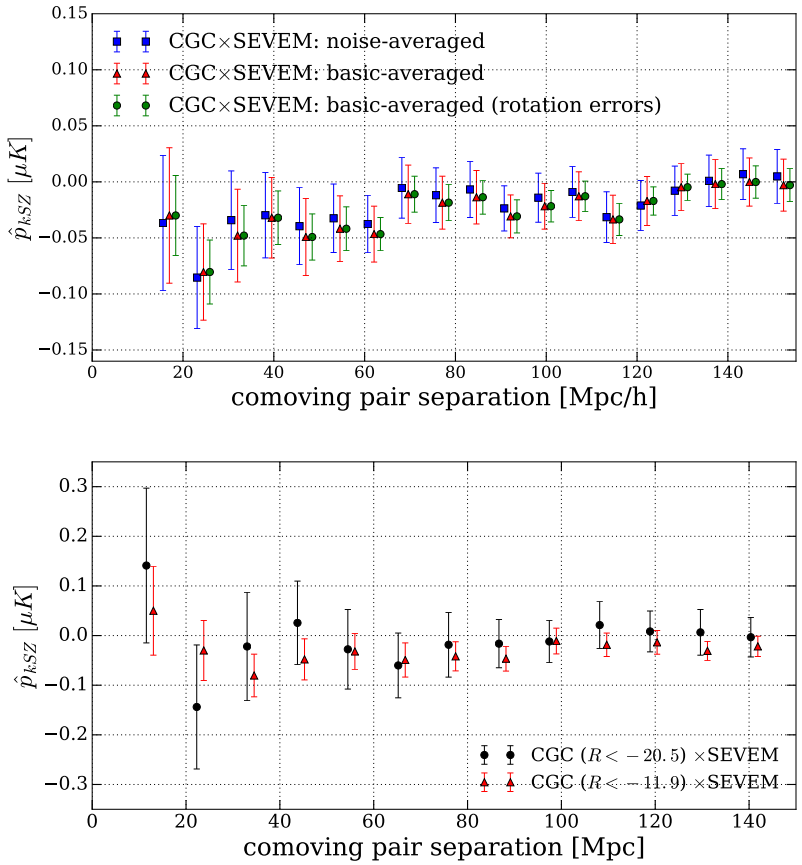

Figure 2.4: Comparisons of the $\hat{p}_{kSZ}$ signal and variance obtained for CGC×SEVEM using an 8 arcmin aperture. Shown in both plots [red triangles] is $\hat{p}_{kSZ}$ using flat-weighing for the pixels, and JK errors for a galaxy sample, such that the absolute R-band magnitude falls within $-28.9 < R < -11.9$. [Left] A comparison of results using different CMB map weighting schemes and covariance estimators, comparing pixels that are noise-weighted [blue square] and flat-weighting [red triangles] with JK error estimates, and flat-weighted pixels with rotation errors, as in [5] [green circles]. To aid comparison with the Planck results, on this plot alone, we express separations in Mpc/h, but use Mpc in all future figures. [Right] A comparison of different luminosity cut-offs for the CGC galaxy sample, such that the absolute R-band magnitude falls within $-28.9 < R < -11.9$ [red triangles] and $-28.9 < R < -20.5$ [black circles]. In both cases, only the brightest galaxy within a 1 Mpc radius is retained to isolate the best central galaxy candidate within a cluster volume.

while reducing potential contamination from satellite galaxies. The stricter selection criteria, especially at lower separations, shifts p_{kSZ} by more than the 1σ relative to that using the conservative criteria. The statistical uncertainties are also increased, consistent with the more aggressive cut decreasing the sample size. At 43 Mpc separation, for example, the errors differ of the stricter cut are larger than the initial sample by a factor of 2.0, while the signal is increased by a factor of 0.5.

In Figure 2.5, we study the robustness of the aperture photometry method to assumptions on aperture size and foreground contamination. We consider fixed angular apertures to range from 3 to 8 arcmins, based on the expectation scaled by the cluster size, $\Theta(\bar{z})$, as given in 2.1. We also consider the redshift-scaled aperture for the WISE and CMASS+LOWZ datasets. Cases where the aperture is incorrectly selected will result in scenarios in which cluster data is being inappropriately selected: for a smaller aperture the outer annulus being differenced, to remove the background CMB, will be contaminated by cluster signal, while for the larger aperture regions with no cluster signal will be included in the averaged aperture temperature leading. In both cases we would anticipate an underestimated signal. For the CGC and WISE samples, focused a lower redshifts we find that the fixed and redshift-varying apertures give largely consistent results. For the CMASS+LOWZ sample that has a higher mean redshift, we find that, particularly for separations between $\sim 100 - 140 Mpc$, the two aperture selection choices give results that vary by $\sim 1\sigma$. The redshift scaled aperture also has larger statistical errors.

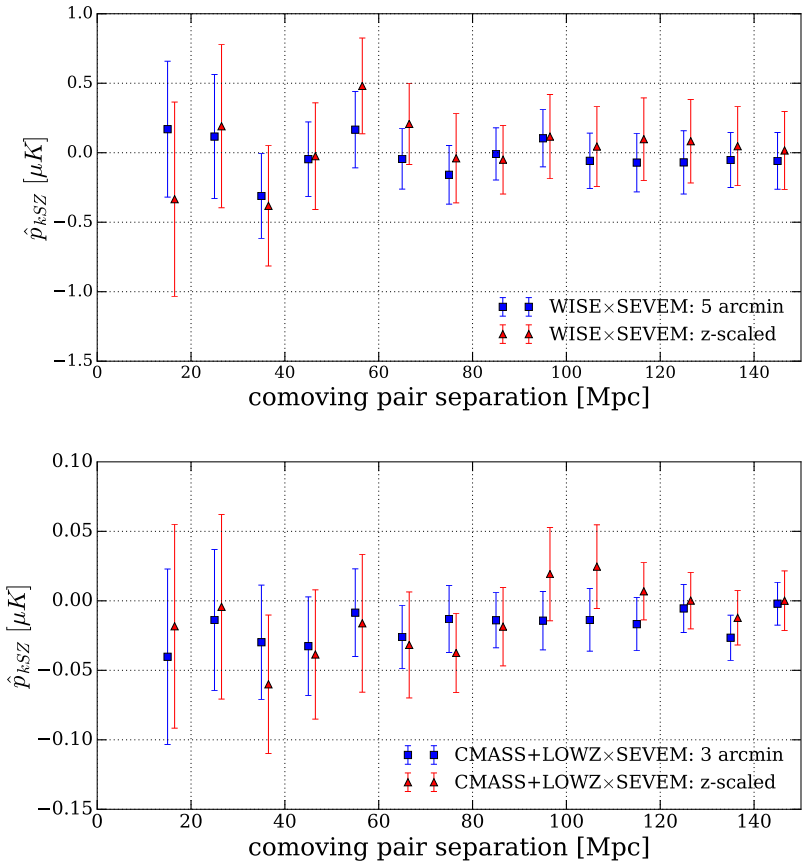

Figure 2.5: Comparisons of the $\hat{p}_{kSZ}$ signal and variance obtained for the SEVEM CMB data and [left] the WISE and [right] CMASS+LOWZ galaxy samples. In each a redshift dependent [blue square] and z-independent [red triangle] aperture, that closely matches the expected angular size of a cluster at each sample's mean redshift.

2.4.3 $\hat{p}_{kSZ}$ signal-to-noise estimates

For each dataset we calculate the signal-to-noise ratio (SNR) [31, 23],

$$\left(\frac{S}{N}\right)^2 = \sum_{ij} \hat{p}_{kSZ}(r_i) Cov^{-1}(r_i, r_j) \hat{p}_{kSZ}(r_j). \tag{2.12}$$

The inverse of an unbiased estimator for some statistical variable x is in general not an unbiased estimator for x^{-1} so we account for the jackknife covariance bias by the

standard correction factor given by

$$Cov^{-1} = \frac{(N_{JK} - N_{bins} - 2)}{(N_{JK} - 1)} Cov_{JK}^{-1}. \tag{2.13}$$

For CGC×SEVEM, Ade et al. [5] consider SNR results (which they denote χ^2_{null}) for a subset of three bins, 15, 38 and 81 Mpc/h, and report 0.3σ and 0.4σ significance for 5 and 8' apertures, respectively. In our analysis, we considered three similar bins, 22, 54, 115 Mpc (for $h = 0.7$ these would denote 15, 38 and 83 Mpc/h) with errors from the rotation method, and found SNR = 1.6 and 2.5, which can be expressed as 0.45 and 0.72σ confidence limits in the $N_{bin} = 3$-dimensional parameter space.

We find bin selection does lead to variations in the SNR. For the 5' case, for example: if we change the third bin from 115 to 108 Mpc we find the SNR shifts from 0.45 to 0.36σ; while adding an additional bin, 87 Mpc or 97 Mpc, leads to an SNR of 1.52σ or 0.25σ, respectively.

As expected, we find that the SNR is markedly lower for JK-estimated errors, consistent with the comparative sizes of the errors shown in Fig 2.3. For the 5' and 8' apertures, and the subset of three bins, at 22, 54, 115 Mpc, the SNR is 0.13 and 0.26σ, and a similar variation depending on bin selected.

To compare the SNR for each of the datasets in the chapter, we avoid an arbitrary subset selection, and consider all bins in the range of comoving separations between 15 and 150 Mpc and use the full covariance between each bin estimated with the JK method. We find that the highest SNR corresponds to the aperture size choice that most closely reflects an expected cluster size, as given in Table 2.1, but is not improved by using the redshift-dependent aperture for the cases with galaxy samples with extended redshifts. For the CGC data, we find SNR of 0.43σ and 1.0σ for the 5' and 8' apertures respectively. For CMASS+LOWZ, we find 0.05 and 0.37σ significance depending whether the redshift-dependent or 3' fixed aperture was assumed. For WISE, we sim-

ilarly find an SNR of 0.02 and 0.04σ for the redshift-dependent and fixed 5' aperture.

2.4.4 Impact of transverse miscentering

In this section we discuss the impact of angular (transverse) offsets of the targeting galaxy from the cluster's center using methods described in §2.3.4.

To create catalogs to further investigate the offset distributions, we take into account the five most likely central galaxy candidates based on the redMaPPer centering probability [38] (considering those candidates with the highest $P_{cen,i}$, where $i = 1$ through 5).

In Figure 2.6, we compare the results for the pairwise estimator found with the both a redMaPPer Brightest Galaxy (BG) catalog (the brightest LRG in the cluster) and a redMaPPer Central Galaxy (CG) catalog (the LRG with the highest centering probability) for moderate to high, $\lambda > 20$, and low richness $5 < \lambda < 20$ cluster samples. In both cases, the results demonstrate that the uncertainty due to miscentering is comparable to the JK statistical error estimates. We find deviations averaged over comoving separations $\sim 15 - 155$ Mpc to be 0.5σ for both the low and high richness SDSS samples, and a maximum deviation of 0.9σ at 35 Mpc and 1.5σ at 25 Mpc, for the low and high richness samples respectively.

As a complementary study, we use the photometric redMaPPer catalog directly, to study miscentering using the Johnston analytic model with the spectroscopic galaxy samples. We inform the Johnston model parameters using the RedMaPPer (RM) data. For our RM SDSS samples, we find f_J is $70 - 75\%$, indicating that selecting brightest

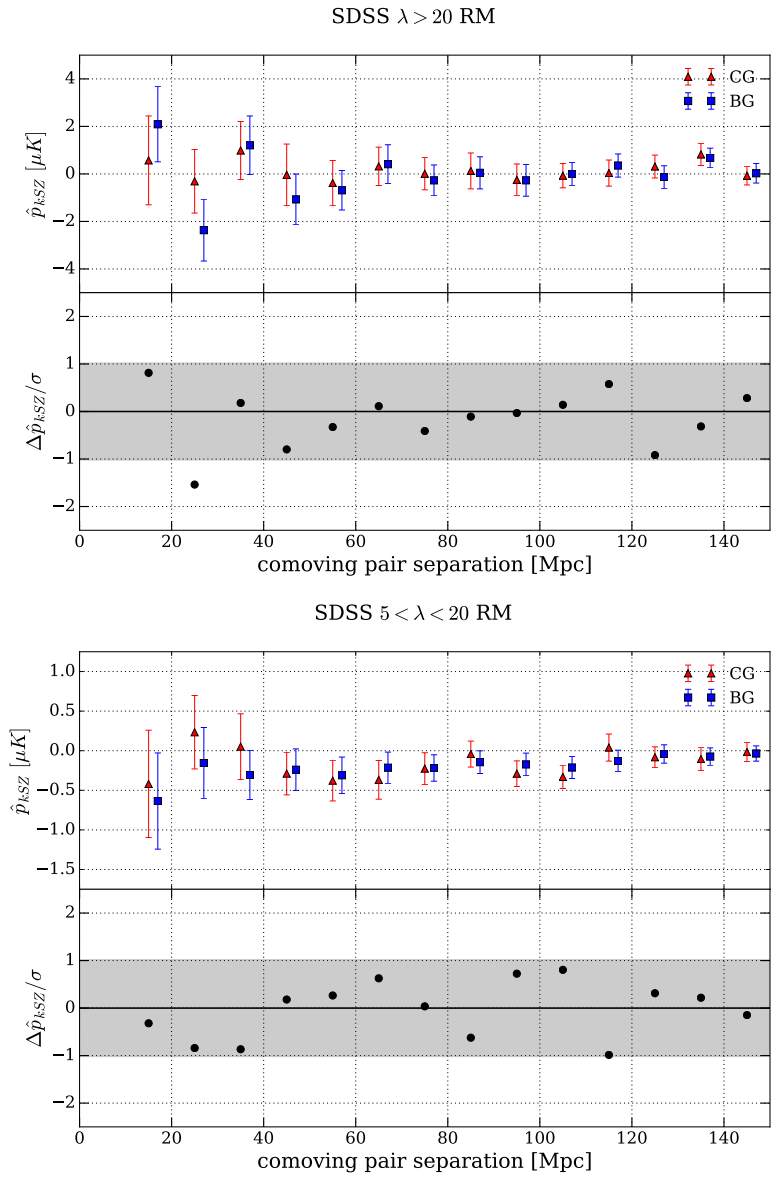

Figure 2.6: $\hat{p}_{kSZ}$ for cross-correlations using SDSS redMaPPer samples for clusters samples with [left panels] $\lambda > 20$ and [right panels] $\lambda < 20$, as summarized in Table 2.1. [Top panels] A comparison of $\hat{p}_{kSZ}$ derived using Central Galaxy catalogs (CG) [red triangle] and corresponding redMaPPer Brightest Galaxy (BG) [blue square] selections. [Lower panels] $\Delta\hat{p}_{kSZ}/\sigma$ is the difference in signal, $\hat{p}_{kSZ,BG} - \hat{p}_{kSZ,CG}$, scaled relative to the JK errors for the CG catalog, to measure the deviation of the signal between the brightest and true central galaxy, relative to the statistical error estimate.

galaxy accurately identifies the cluster center $70-75\%$ of the time. The value of σ_J is estimated by computing d and $P(d)$ based on the off-centering distribution given by

$$P(d_{ij}) = P_{cen,i} P_{mem,j} \Pi_k (1 - P_{mem,k}), \tag{2.14}$$

in which we normalize by the richness-dependent cutoff radius $R_c(\lambda)$ in equation (2.2), and fitting those to the f_J given by the Johnston model above. This yields estimates of the σ_J in units of Mpc/h: 0.28 for the SDSS RM with $\lambda > 20$, 0.35 for the SDSS RM with $\lambda < 20$, and 0.34 for the LOWZ+CMASS DECaLs sample.

Based on these results, we consider $\sigma_J = 0.3$ Mpc/h, and 0.5 Mpc/h, $f_J = 0.75$ and $h = 0.6731$. We determine the relative importance of miscentering systematics to the statistical uncertainties by considering the covariances introduced in 50 offset trials, based on the same generating seed, in which a different $(1 - f_J) = 25\%$ of the cluster locations shifted by the same random Gaussian displacement scaled by, standard deviation, σ_J. For WISE, only galaxies with $z > 0.03$ are shifted, as the characteristics of the very low redshift sources are better known and miscentering is expected to be less of an issue, while concurrently the model would induce large angular offsets. In Figure 2.7, we present the results of these offset trials for different LSS and CMB data pairings. The variance in the pairwise signal between each of the 50 runs generated by the offsets are compared to the JK statistical errors from the jackknife analyses. The results show that, while miscentering does not introduce a systematic shift in the pairwise signal, it does induce a significant enhancement to the kSZ statistical error budget. Averaged over the pairwise statistic at all separations ($\sim 15 - 150$ Mpc), for CGC we find miscentering uncertainties are 0.7σ for $\sigma_J = 0.3 Mpc/h$. For the CMASS+LOWZ, we find 0.6σ and for WISE, 0.4σ. We find the maximum deviations occur for the CGC at ~ 100 Mpc, of 0.7σ, for WISE at 65 Mpc, of 0.5σ, and for CMASS+LOWZ 0.8σ at 155 Mpc. Deviations at small separations where the kSZ effect is strongest are most important as a source of systematic uncertainty and in all cases the variation in $\hat{p}_{kSZ}$ due to miscenter-

ing is significantly greater below separations of 60 Mpc. It is interesting to note that while both JK and miscentering errors decrease with increased sample size, progressing from WISE, to CGC and CMASS+LOWZ, the miscentering uncertainties concurrently become a larger fraction of the error budget, suggesting that they will not be ameliorated in future surveys simply as a result increased galaxy samples.

2.4.5 Impact of photometric redshift errors

Photometric redshift errors can themselves be a source of contamination to the kSZ signal. To analyze this prospect with the DECaLs RMCG sample 50 realizations were created in which galaxy radial positions had random offsets applied to the approximately half of the sample which have photometric instead of spectroscopic redshifts, sampled from a Gaussian of width corresponding to the error given for the photometric redshifts. Figure 2.8 gives a comparison of the variance in the realizations modeling the photometric redshift errors to the differences induced by shifting from the most likely central galaxy (CG) to the brightest galaxy (BG) catalog and the JK statistical errors. At comoving separations exceeding 175 Mpc, where the kSZ signal becomes approximately null, and the JK errors are very small, photometric redshift errors dominate.

At smaller separations, $<\sim$50 Mpc, photometric redshifts and miscentering both make significant contributions to the error budget, with differences between the BG and CG data being the larger. In the range of separations up to 50 Mpc, miscentering errors are comparable to the JK statistical errors, while photometric redshift errors constitute an average 0.28σ, with a peak value of 0.34σ at 10 Mpc.

2.5 Conclusions

The kSZ temperature deviation in galaxy clusters could provide a powerful probe of dark energy and modifications to gravity on a cosmic scale, distinct from galaxy lensing and clustering, that are principal science drivers for upcoming large scale structure surveys. Current approaches center on kSZ pairwise momentum estimates between clusters, obtained through cross-correlation of the CMB data with galaxy samples that are used as cluster proxies to determine accurate pairwise separations. Improved resolution and frequency coverage in the next generation of sub-arcminute scale CMB measurements, twinned with increased breadth and depth in the next generation of LSS surveys, pave the way for significant improvements in kSZ signal extraction, but only if astrophysical and analysis systematics are understood and mitigated at a commensurate level.

In this chapter, the impact of a number of modeling assumptions and potential systematic uncertainties that can be introduced in the estimation of the pairwise kSZ correlation have been considered. Planck and WMAP CMB data are used in combination with galaxy samples from SDSS, WISE, and DECaLs surveys.

In comparing covariance estimation techniques, the JK method was found to be more conservative than random rotations. A sensitivity to aperture size selection was found for both methods, and most pronounced for the galaxy samples distributed over extended redshift ranges. In contrast, a comparison of flat- vs. noise-weighting CMB maps was found to have little impact on the pairwise statistic from current Planck data.

We also found negligible differences in results for the SEVEM and LGMCA maps, for the same galaxy sample, suggesting that the aperture photometry method was robust to the differences in residual foreground removal. The signal-to-noise ratio was evaluated for the CGC, CMASS+LOWZ and WISE samples. To provide context with other

analyses in the literature, we considered the sensitivity to the selection of subsets of data and to aperture size. While none of the datasets leads to a new significant detection of the kSZ effect, we did find that the greatest SNR was when the fixed aperture size most closely reflect the expected angular size of a cluster for the sample. The impact of miscentering was considered using two complementary techniques: the Johnston analytical offset model and a redMaPPer-based comparison of signals assuming samples of the brightest (BG) versus the most likely central (CG) galaxy per cluster. The redMaPPer data was used to inform the parameter choices used in Johnston model [40]; for all samples, we found that ∼25% of the predicted clusters had brightest galaxies that were offset with a Raleigh distribution with a peak ∼0.3 Mpc$/h$. In both the direct comparison of BG and CG redMaPPer catalogs and Johnston analytic model, miscentering leads to additional uncertainties equivalent to a significant fraction of the JK error budget. Using redMaPPer, we find deviations averaged over comoving separations $\sim 15-150$ Mpc to be 0.5σ for both the low and high richness SDSS samples. Using Johnston offset modeling, with mean offset 0.3 Mpc$/h$, we find 0.4σ for WISE, and 0.6σ for CMASS+LOWZ, and 0.7σ for CGC.

The DECaLs redMaPPer sample was used to compare photometric redshift and miscentering errors in tandem. Miscentering was found to be the dominant of the two uncertainties at < 50 Mpc, where the kSZ signal is largest, with deviations at the $\sim \sigma$ level. Photometric redshift errors were also not negligible however, as noted in [72] and [45], with a mean deviation of 0.3σ.

This work provides quantitative evidence that uncertainties in cluster centering (in terms of both transverse and radial (redshift) location) can introduce significant uncertainties, comparable to current statistical errors in the kSZ pairwise signal. Order of magnitude improvements in instrumental precision and survey size anticipated with the

next generation of CMB and LSS surveys will allow smaller separations, at which the kSZ signal is largest, to be accessible with photometric surveys. Miscentering uncertainties will need to mitigated, however, so as to not dominate the error budget. This work suggests a combination of spectroscopic redshift precision and multiple cluster galaxy populations from photometric surveys, such as will be obtained with Euclid and WFIRST, and in overlapping regions of the DESI and LSST surveys, may be optimal to appropriately constrain both transverse and radial cluster positioning. Similarly this suggests implications for miscentering in kSZ analyses with simulations based on upcoming surveys due to the fact that even the true brightest cluster galaxy does not always trace the location of the projected center of electron distribution.

Looking forward, a variety of techniques may be employed to better extract the kSZ signal, such as the application of matched-filter estimators [48] and Gaussian constrained realizations [8] that will improve kSZ decrement estimation and also reduce reliance on cluster centering. Improved precision in cluster centering may also be achieved through using additional data, such as weak lensing information [32]. Going beyond this, multi-frequency CMB temperature and polarization data will provide opportunities to extend from precise pairwise momenta measurements to both pairwise, and individual, cluster velocities to fully realize the potential of the kSZ effect for cosmology. This will require concurrent measurements of cluster optical depth with an additional set of astrophysical and analysis assumptions that can contribute to the error budget [11, 51]. While we have considered pairwise correlations for comoving separations between 15 and 150 Mpc, to fully understand the impact of analysis assumptions on signal extraction at scales where the signal is largest, clearly other considerations such as velocity biasing [10] and non-linear clustering will also need to be understood and characterized in order to convert the extracted signal to a peculiar velocity and cosmological model. Alternative approaches, such as using three-point statistics of all large scale structure

[34, 24], also open up kSZ science that may not rely on precise cluster identification. We leave detailed consideration of these next steps to future work.

Acknowledgments

We thank Eduardo Rozo and Eli Rykoff for providing the redMaPPer catalogs used in this analysis, and Wenting Wang and Carlos Hernández-Monteagudo for sharing a CGC-derived catalog developed for the Planck kSZ analysis in [5]. We are grateful to Nicholas Battaglia, Francesco De Bernardis, Hanako Hoshino, Michael Niemack and Eve Vavagiakis for helpful conversations in the course of this work. The work of VC and RB is supported by NASA ATP grant NNX14AH53G, NASA ROSES grant 12-EUCLID12- 0004 and DoE grant DE-SC0011838.

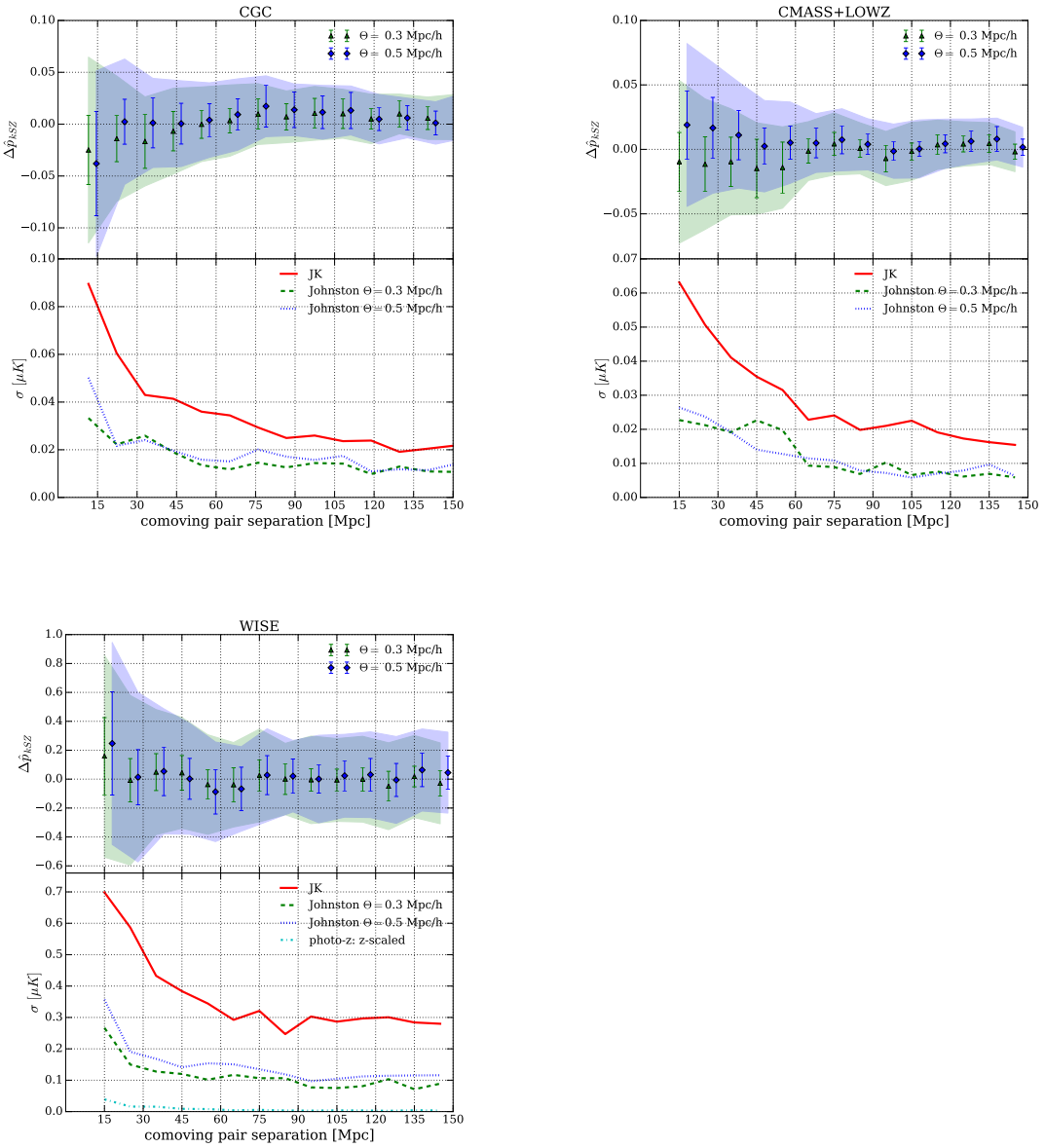

Figure 2.7: A comparison of uncertainties arising from the Johnston miscentering model relative to JK errors for the [left] CGC, [center] CMASS+LOWZ, and [right] WISE samples, using aperture choices of 8 arcmin, 3 arcmin, and z-scaled respectively. [Upper panel] $\Delta\hat{p}_{kSZ}$ is computed by $\langle\hat{p}_{kSZ,offset_n} - \hat{p}_{kSZ}\rangle$, where n is each of the 50 trials for $\sigma_J = 0.3$ [green triangle] and 0.5 Mpc/h [blue diamond]. The variance for each offset size is the r.m.s. difference between the individual 50 offset trials and the original signal. The shaded regions represent the JK variance of the original signal. [Lower panel] A comparison of the variance due jackknife resampling [red full], the Johnston offset model with an offset width 0.3 Mpc/h [green dashed] and 0.5 Mpc/h [blue dotted], for the original brightest-galaxy samples.

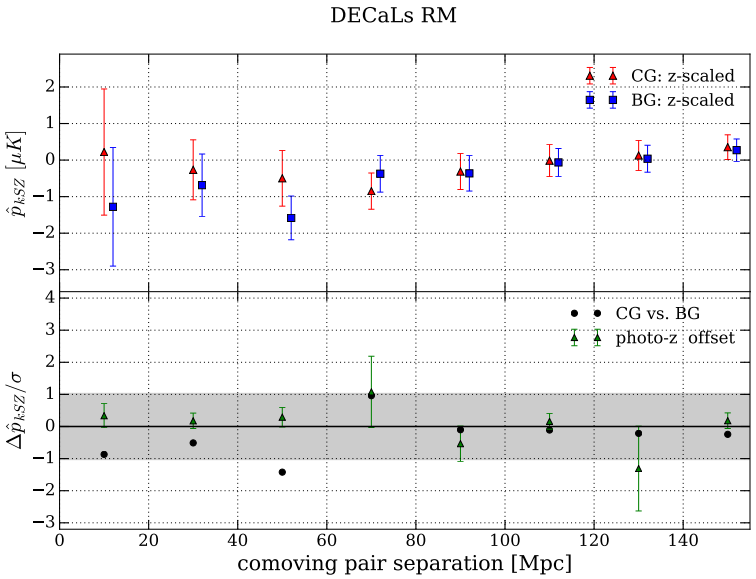

Figure 2.8: A comparison of the kSZ signal from the brightest galaxy (BG) and central galaxy (CG) selections from DECaLs redMaPPer data using a z-dependent aperture. As in Figure 2.6, [Top panel] a comparison of $\hat{p}_{kSZ}$ derived using Central Galaxy catalogs (CG) [red triangle] and corresponding redMaPPer Brightest Galaxy (BG) [blue square] selections. [Lower panel] $\Delta\hat{p}_{kSZ}/\sigma$ is the difference in signal, $\hat{p}_{kSZ,BG} - \hat{p}_{kSZ,CG}$, scaled relative to the JK errors for the CG catalog [black circle]. The lower panel also demonstrates the variance introduced by photometric redshift ('photo-z') errors on the kSZ signal. 50 trials are created with random offsets to cluster locations, based a Gaussian width corresponding to the photometric redshift error given for the CG sample. The average signal and variance of the 50 trials is shown as a ratio of the JK statistical errors [green triangle].

CHAPTER 3

THE ATACAMA COSMOLOGY TELESCOPE: DETECTION OF THE PAIRWISE KINEMATIC SUNYAEV-ZEL'DOVICH EFFECT WITH ACTPOL AND SDSS DR15 GALAXIES

3.1 Introduction

Understanding the origins of accelerated cosmic expansion, and thus, dark energy, [58, 61] is one of the central goals for modern cosmology. This chapter, along with a companion paper, Vavagiakis et al. (herein V20), focuses on a comparatively recent technique to measure the peculiar motions of the largest gravitationally collapsed cosmological structures, galaxy clusters, and use their redshift evolution and spatial correlation to constrain the properties of dark energy, and components of the dark sector, more generally, including the properties of massive neutrinos. This work is currently under review in the ACT collaboration prior to be being submitted for publication.

As CMB photons traverse through the galaxy clusters, the most massive bound objects in the universe today, they interact with the hot cluster gas. The Dopper-shift distortion in the CMB caused by the peculiar motions of galaxy clusters relative to the Cosmic Microwave Background (CMB) rest-frame is known as the kinetic Sunyaev-Zel'dovich (kSZ) effect [75].

Concurrently with the kSZ, the CMB photons are also heated up by the cluster gas, the thermal Sunyaev-Zel'dovich effect (tSZ). The tSZ effect has a characteristic frequency dependence, meaning it can be isolated through the use of multi-frequency measurements. The kSZ effect is an order of magnitude smaller and does not have a distinctive variation with frequency which make its detection, and separation tSZ and

dust emission foregrounds, challenging.

Pairwise motions caused by the inward gravitational pull of galaxies can be utilized to extract the kSZ. The pairwise statistic is a useful approach to extracting kSZ signals because of its dependence on linear differences of measured temperatures on the sky at the positions of clusters, averaging out contaminating signals like the tSZ signal and dust emission. The pairwise kSZ momentum, sensitive to both the cluster peculiar velocity and optical depth, has the shown to have the potential to probe the LSS growth rate, providing insights to the evolution of dark energy, cosmic modifications to gravity over cosmic time, and constraints on the sum of the neutrino masses [16, 54, 53, 26].

Extraction of the kSZ signal is aided by using galaxy surveys to provide proxies to identify and locate the clusters [43, 41, 25, 46, 74]. The first statistical detection of the kSZ signal in CMB maps was made by the Atacama Cosmology Telescope and SDSS collaborations by estimating the mean pairwise cluster momentum from a sample of clusters traced by their bright central galaxies in the Sloan Digital Sky Survey (SDSS) [29]. This measurement has since been improved in a 4.1σ measurement using improved data from ACT and the BOSS-SDSS DR11 [23]. Detections using the same estimator have been reported by the Planck collaboration using galaxies from SDSS [5], and the South Pole Telescope collaboration using galaxies from the Dark Energy Survey [72]. The latter analysis' 4.2σ detection illustrated that the pairwise kSZ signal can be extracted using photometric data once the redshift uncertainty is accounted for.

Various statistical detection techniques have been successfully employed to measure the kSZ effect, including velocity template cross-correlation methods and map-squaring techniques. [69, 5]. Schaan et al. (2016) [69] measured the amplitude of the kSZ signal as a function of radius and reported 2.9σ and 3.3σ evidence of the kSZ using two different velocity reconstruction methods. Hill et al [34] used foreground-cleaned CMB

temperature maps constructed from multi-frequency Planck and WMAP data and galaxy measurements from the Wide-field Infrared Survey Explorer (WISE) [78] to yield a 3.8–4.5 σ kSZ detection, depending on the galaxy bias constraints. This method has the advantage of not requiring redshift estimates for individual clusters, allowing for the use of photometric data without treating redshift uncertainties.

Our work is laid out as follows: In Section 3.2, we describe the properties the ACT-Pol+Planck CMB map we use for our analysis, as well as those of the SDSS galaxy samples we cross-correlate with it. Next in Section 3.3, we lay out the formalism for the pairwise estimator, the covariance techniques, the signal-to-noise and τ estimation, and the cluster centering estimation. In Section 3.4, we discuss our results, motivating the analysis approach, presenting the pairwise kSZ detections, and mis-centering and systemics study. These findings are drawn together in the Conclusion, Section 3.5.

3.2 Datasets

We extract the pairwise kSZ signal by cross-correlating our galaxy samples from the Sloan Digital Sky Survey Baryonic Acoustic Oscillation Survey (SDSS BOSS) DR15 catalog with CMB data primarily from the Atacama Cosmology Telescope (ACT). Here we discuss the selection for this data.

3.2.1 ACTPol data

We use four CMB datasets that combine ACTPol and Planck data in our analyses.

A component-separated internal linear combination map (referred to as S16 ILC)

uses four seasons of ACTPol observations, from 2013-2016, covers 2,089 sq. deg with the BOSS survey (1633 sq. deg. in the BOSS-N field and 456 sq. deg. in the DEEP56 region) and Planck [49]. A complementary dataset uses ACTPol night time observations from 2013-2016 co-added with Planck (referred to as S16 f150). The final two datasets co-add ACTPol data that includes observations from the 2017 and 2018 seasons and data from daytime observations with Planck at two separates frequencies, centered roughly at 98GHz and 150 GHz (referred to as S18 f090 and S18 f150 respectively). These datasets cover $\sim$ 21,000 sq. deg. of the sky. By including data at multiple 150 GHz and 90 GHz and component separated maps with foregrounds identified and removed, we seek to mitigate the likelihood of thermal SZ contamination. The CMB maps have point source and galactic plane mask, and a noise threshold cut of 45 μK, as discussed in more detail in V20.

3.2.2 SDSS data

In this analysis we select galaxies overlapping with the CMB region from the 15^{th} Data Release of the Baryon Oscillation Spectroscopic Survey (BOSS-SDSS DR15) [6]. We impose the luminosity selection specifying luminous red galaxies (LRGs) from the CMASS and LOWZ subsamples based on the criteria given in the BOSS Galaxy Target Selection [1]. We compute the k-corrected luminosities [13] and select luminous red galaxies based on *r*-band Petrosian magnitudes. The SDSS query to obtain the galaxy sample is provided in V20.

We consider five different cumulative luminosity bins from $L > 5.4 \times 10^{10} L_{\odot}$ to $L > 16.3 \times 10^{10} L_{\odot}$, as well four different disjoint luminosity bins from in the same range. We summarize the properties of these nine samples, including the equivalent

[1] *https:/www.sdss.org/dr14/algorithms/boss_galaxy_ts*

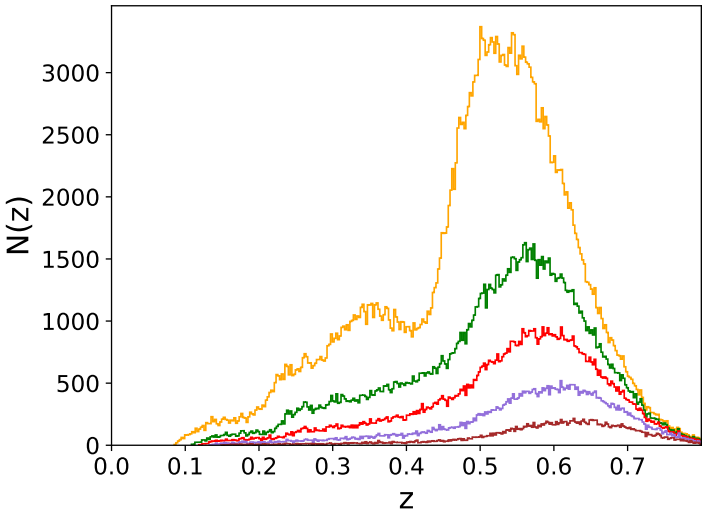

Figure 3.1: The number of galaxies as a function of redshift for the S18 f150 map and DR15 galaxy samples for each of the cumulative luminosity samples used in the analysis. From top to bottom these show the samples with luminosities exceeding 5.4 [orange], 8.6 [green], 10.4 [red], 12.8 [purple], and 16.3 [brown]$\times 10^{10} L_{\odot}$, respectively.

mass ranges, the redshift dispersion and the number of galaxies included, in Table 3.1 and Figure 3.1. The approach to obtain the luminosity-mass equivalence is described in V20. With these luminosity cuts we analyze results using 342,951 galaxies out of the total DR15 sample size of 602,461.

L ($10^{10} L_\odot$)	M M_{200} ($10^{13} M_\odot$)	S16 ILC			S16 f150			S18 f150 & S18 f090		
		N_{gal}	$\bar{z}$	σ_z	N_{gal}	$\bar{z}$	σ_z	N_{gal}	$\bar{z}$	σ_z
$L > 5.4$	$M > 0.79$	190,896	0.50	0.13	287,035	0.49	0.13	342,951	0.49	0.13
$L > 8.6$	$M > 1.97$	96,806	0.52	0.13	144,784	0.52	0.13	172,409	0.52	0.13
$L > 10.4$	$M > 2.93$	57,156	0.55	0.12	85,360	0.54	0.13	101,393	0.54	0.13
$L > 12.8$	$M > 4.58$	28,747	0.57	0.12	42,992	0.57	0.12	50,975	0.57	0.12
$L > 16.3$	$M > 7.81$	11,696	0.60	0.11	17,286	0.59	0.12	20,457	0.59	0.11
$5.4 < L < 8.6$	$0.79 < M < 1.97$	94,090	0.47	0.12	142,251	0.47	0.12	170,542	0.47	0.12
$8.6 < L < 10.4$	$1.97 < M < 2.93$	39,650	0.49	0.13	59,251	0.49	0.13	71,016	0.49	0.13
$10.4 < L < 12.8$	$2.93 < M < 4.58$	28,409	0.52	0.12	42,368	0.52	0.12	50,418	0.52	0.12
$12.8 < L < 16.3$	$4.58 < M < 7.81$	17,051	0.55	0.12	25,706	0.55	0.12	30,518	0.55	0.12

Table 3.1: Summaries of the nine luminosity-determined samples analyzed in this chapter. The equivalent mass ranges, M_{200}, the number of galaxies, N_{gal}, the mean redshift, $\bar{z}$, standard deviation, σ_z, and the aperture size of a 1 Mpc scale at $\bar{z}$, $\Theta(\bar{z})$ are given in each case.

3.3 Formalism

3.3.1 Pairwise estimator

The CMB temperature shift induced by the galaxy cluster's peculiar motion is given by [76],

$$\frac{\delta T_{kSZ}}{T_0}(\hat{r}) = -\int dl\, \sigma_T\, n_e \frac{\mathbf{v}\cdot\hat{\mathbf{r}}}{c} \tag{3.1}$$

where n_e is the electron number density and σ_T is the Thomson cross-section. A positive peculiar velocity, $\mathbf{v}$, relates to motion away from the observer, so induces a negative kSZ effect. If the kSZ signal is dominated by a single cluster along the line of sight, the kSZ

temperature for each cluster is given by

$$\delta T_i(r^i, z^i, \sigma_z, \Theta) = T_{AP}(r^i, \Theta) - \bar{T}_{AP}(r^i, z^i, \Theta, \sigma_z), \tag{3.2}$$

where $T_{AP}(r^i, \Theta)$ is the kSZ temperature at the angular position of the i^{th} galaxy with an aperture size Θ, estimated by aperture photometry (AP)

$$T_{AP}(r^i, \Theta) = \frac{\sum_{\in \text{disk}} f_{pix} T_{pix}}{\sum_{\in \text{disk}} f_{pix}} - \frac{\sum_{\in \text{annulus}} f_{pix} T_{pix}}{\sum_{\in \text{annulus}} f_{pix}}. \tag{3.3}$$

Here the AP temperature is obtained by averaging over the temperatures of pixels in the disk of size Θ and an annulus of $\sqrt{2}\Theta$, around the galaxy identified as a proxy of the cluster center, position r_i, including fractional weightings, f_{pix}, for pixels that are only partially in each area. $\bar{T}_{AP}$ is the averaged aperture temperatures over all cluster in a Gaussian distributed redshift range centered on the cluster, to account for potential redshift evolution in the thermal SZ signal:

$$\bar{T}_{AP}(r^i, z^i, \Theta, \sigma_z) \quad = \quad \frac{\sum_j T_{AP}(r^i, \Theta) \exp\left(-\frac{(z_i - z_j)^2}{2\sigma_z^2}\right)}{\sum_j \exp\left(-\frac{(z_i - z_j)^2}{2\sigma_z^2}\right)} \tag{3.4}$$

The sum is over all galaxies, j, in the same redshift bin as cluster i, and we take $\sigma_z = 0.01$ as in work by the Planck team [5].

We implement the pairwise momentum estimator [25], in which a signal represents the correlation of cluster velocities,

$$\hat{p}(r) = -\frac{\sum_{i<j} (\delta T_i - \delta T_j) c_{ij}}{\sum_{i<j} c_{ij}^2}, \tag{3.5}$$

where the sum is over all cluster pairs, located at positions $\mathbf{r}_i = \{\hat{\mathbf{r}}_i, z_i\}$ and $\mathbf{r}_j = \{\hat{\mathbf{r}}_j, z_j\}$, separated by a distance $r = |\mathbf{r}_{ij}| = |\mathbf{r}_i - \mathbf{r}_j|$, and with $\hat{\mathbf{r}}$ the unit vector in the direction of $\mathbf{r}$. δT_i represents the relative kSZ temperature The weights c_{ij} are the geometrical factor that accounts for the alignment of a pair of clusters i and j along the line of sight [23], given by

$$c_{ij} = \hat{r}_{ij} \cdot \frac{\hat{r}_i + \hat{r}_j}{2} = \frac{(r_i - r_j)(1 + cos\alpha)}{2\sqrt{r_i^2 + r_j^2 - 2 r_i r_j cos\alpha}} \tag{3.6}$$

where α is the angle between $\hat{r}_i$ and $\hat{r}_j$. We update the approaches used [17], which analyzed Planck SEVEM maps in HEALPix format, and [23]. The pipeline used in this work utilizes Pixell [2] subroutines to analyzing the CMB map. The codes are parallelized, in python, and will be made publicly available.

The assumptions going into the kSZ extraction undertaken in this work include some analytic differences from that in previous work, y including fractional pixel weighting, reprojecting the pixellation of the submap, and implementing cluster-centered, instead of pixel-centered, aperture photometry. We discuss these differences and their respective implications for the signal extraction in Appendix A.1.

3.3.2 Covariance estimation

For the analysis of both the S16 S16 ILC and S18 S18 f150 CMB maps, we consider jackknife and bootstrap approaches to obtain estimates for the pairwise velocity signal covariance. For the S16 S16 ILC map we also utilize simulations of the map noise [3] as a distinct, complementary approach to estimate the covariance estimation. In using jackknife resampling (JK), we bin the clusters into N_{JK} subsamples, removing each subsample exactly once, and each time computing the pairwise estimator according to the remaining $(N_{JK} - 1)$ subsamples. The covariance matrix is then given by

$$\hat{C}_{ij} = \frac{N_{JK} - 1}{N_{JK}} \sum_{\beta=1}^{N_{JK}} (\hat{\bar{p}}_i^{\beta} - \bar{p}_i)(\hat{\bar{p}}_j^{\beta} - \bar{p}_j), \tag{3.7}$$

where, for the r_i^{th} separation bin, $\hat{\bar{p}}_i^{\beta}$ is the signal extracted from the β^{th} JK sample and $\bar{p}_i$ is the mean of the N JK samples [73]. The inverse covariance matrix is generally a biased estimator true inverse covariance. We correct for this bias by multiplying the inverse

[2] https://github.com/simonsobs/pixell

[3] Choi S., et al., 2020, in preparation

covariance by $(N_{JK} - K - 2)/(N_{JK} - 1)$, where K is the number of comoving separation bins. For our analysis $N_{JK} = 1,000$ and $K = 19$ [23, 31]. Bootstrap resampling is achieved by randomly sampling galaxies with replacement while maintaining the length of the catalog (after applying the luminosity cut) constant. The pairwise estimator is then evaluated b times over a list of galaxies of length N Pairs of repeated galaxies (a consequence of allowing resampling with replacement) are ignored as they have null separations and are not physical. The covariance matrix is then computed as the sample variance of the pairwise estimator applied over the b replicant catalogs

$$\hat{C}_{ij} = \frac{1}{b-1} \sum_{\beta=1}^{N} (\hat{p}_i^\beta - \bar{p}_i)(\hat{p}_j^\beta - \bar{p}_j), \tag{3.8}$$

Convergence tests show that standard errors estimated using the sample variance for $b = 1,000$ replicants are within 5% of the variances obtained by using the 68 percentile from the mean.

Finally, for the S16 ILC we use variance of the CMB noise signals obtained in 450 simulations produced in [19] and generated using the pipeline described in [4] (specifically, we use version $v1.0.0_{rc}$ for the simulations).

3.3.3 Signal to Noise and τ estimates

We compare our pairwise kSZ momentum measurements to theoretical predictions using a modified version of the CAMB code [47] that calculates the mass-averaged pairwise velocity, v, given by a linear theory laid out in Mueller et al [53, 54]:

$$\hat{p}(r) = -\frac{T_{CMB}}{c} \tau v(r), \tag{3.9}$$

where τ is an effective measure of the cluster optical depth mass-averaged over the cluster sample. For the theoretical predictions, we assume a Planck cosmology for a flat

[4] Choi S., et al., 2020, in preparation

universe [4]: $\Omega_b h^2 = 0.02225$, $\Omega_c h^2 = 0.1198$, $H_0 = 67.3 kms^{-1}Mpc^{-1}$, $\sigma_8 = 0.83$, $n_s = 0.964$. We translate the observational galaxy luminosity cuts to cluster mass cuts using mass-luminosity relationship described in V20. The theoretical pairwise momentum predictions for different τ values are compared with the data to compute the best fit τ value with the minimum χ^2:

$$\chi^2(\tau) \quad = \quad \sum_{ij} \Delta\hat{p}_i(\tau)\hat{C}^{-1}_{ij}\Delta\hat{p}_j(\tau), \tag{3.10}$$

with

$$\Delta\hat{p}_i(\tau) = \hat{p}^{th}_i(\tau) - \hat{p}^{obs}_i, \tag{3.11}$$

where $\hat{p}^{th}_i$ is the theoretical kSZ pairwise momentum estimate obtained from the theoretical pairwise velocity prediction using the cosmological model separation r_i and the assumed τ value and $\hat{p}^{obs}_i$ are the measurements from the ACT and SDSS data.

For each χ^2 value, we also consider the Probability-To-Exceed (PTE), that is the probability of obtaining a higher χ^2 value than the one achieved,

$$PTE = \int_{\chi^2}^{\infty} \chi^2_m(x)dx, \tag{3.12}$$

where χ^2_m is the χ^2 distribution for m degrees of freedom under the assumption of the number ΛCDM model [9]. Unlikely events, or those in tension with theory given the errors, are signified by a low PTE. Finally, we also compute the signal-to-noise ratio (SNR) using the best fit τ based on the theoretical predictions

$$\mathrm{SNR}(\tau) = \sqrt{\sum_{ij} \hat{p}^{th}_i(\tau)\hat{C}^{-1}_{ij}\hat{p}^{th}_j(\tau)}. \tag{3.13}$$

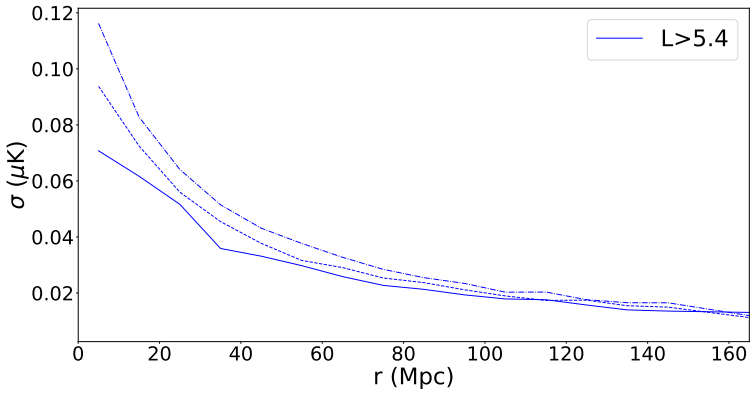

Figure 3.2: Comparison of the 1σ errors obtained from the S16 ILC $L > 5.4 \times 10^{10} L_{\odot}$ sample obtained from simulations [full], jackknife [dashed] and bootstrap [dash-dotted] methods.

3.4 Analysis

3.4.1 Covariance Estimation

In Fig. 3.2 we present a comparison of the JK, simulation, and bootstrap errors for the $L > 5.4 \times 10^{10} L_{\odot}$ galaxy sample and the S16 ILC map. We find that the error estimates become broadly similar at larger separations, r. The JK estimates are the most conservative, followed by the bootstrap, and the simulations, respectively. At $r = 45 Mpc$ the JK and bootstrap errors are respectively 14% and 27% larger than those estimated from the simulations.

In Fig. 3.3 we compare how the errors evolve with luminosity bin and with galaxy sample. We find that the trends in uncertainties are largely driven by sample size, with a $\sqrt{N}$ dependence, consistent with statistically dominated variances. For the S16 ILC sample we find the error at $r = 45 Mpc$ (coincident with the peak predicted k_{SZ} signal), is 0.038 for the $L > 5.4 \times 10^{10} L_{\odot}$ sample versus 0.202 for $L > 12.8 \times 10^{10} L_{\odot}$ with a factor of 6.5 difference in sample size (190,000 versus 29,000 respectively). A similar fractional

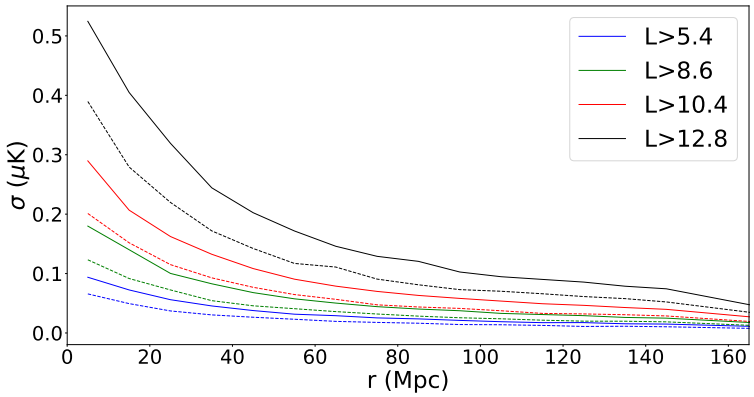

Figure 3.3: Comparison of the 1σ jackknife estimated errors for the S16 ILC [full] and S18 f150 [dashed] maps for the five cumulative luminosity cut samples (L in units of $10^{10}L_{\odot}$).

difference is seen in the S18 f090 with errors of 0.026 for the $L > 5.4 \times 10^{10}L_{\odot}$ sample versus 0.14 for $L > 12.8 \times 10^{10}L_{\odot}$ while the galaxy sample decreases by a factor of 7 (from 342,000 to 50,000). For $L > 5.4 \times 10^{10}L_{\odot}$, we find a decrease in uncertainty of a factor of 0.7 at $r = 45Mpc$ for the S18 f150 map versus the S16 ILC , consistent with the increase in the galaxy sample size N_{gal} by a factor of 1.8 (340,000 relative to 191,000).

In Fig. 3.4 we show the correlations between the signal across the 19 galaxy separation bins. At large separations, as was found in find [23], the pairwise signals are highly correlated across the spatial bins. To improve the conditioning of the covariance matrix we coarsen the bins at large separations. For the analysis, we consider nineteen bins, with fifteen bins of width 10 Mpc, out to separations of r = 150Mpc and, at larger separations, four broader bins centered on separations r =175, 225, 275 and 355 Mpc. We find stronger correlations between adjacent and nearby bins for the lower luminosity cuts, and between bins at high separations across all luminosity cuts, consistently for both JK and simulation-derived covariances.

3.4.2 kSZ Pairwise Correlation

In Figs. 3.5 we present the pairwise kSZ measurements for S16 f150 and S16 ILC ACTPol-Planck CMB maps with the cumulative and disjoint luminosity bins derived from the SDSS DR15 galaxy samples. Results for S18 f150 and S18 f090 are presented in Fig. 3.6. While data out to 395Mpc are utilized in our analysis, for convenience, these plots focus on the cluster separations out to 150 Mpc for clarity, where the kSZ correlation is most pronounced.

The four cumulative luminosity bins (ranging between $L > 5.4$ and $L > 12.8 \times 10^{10} L_{\odot}$) show a pairwise momentum profile with a negative signal amplitude reaching a maximum at separations around 45 and 55 Mpc. The negative amplitude is indicative of

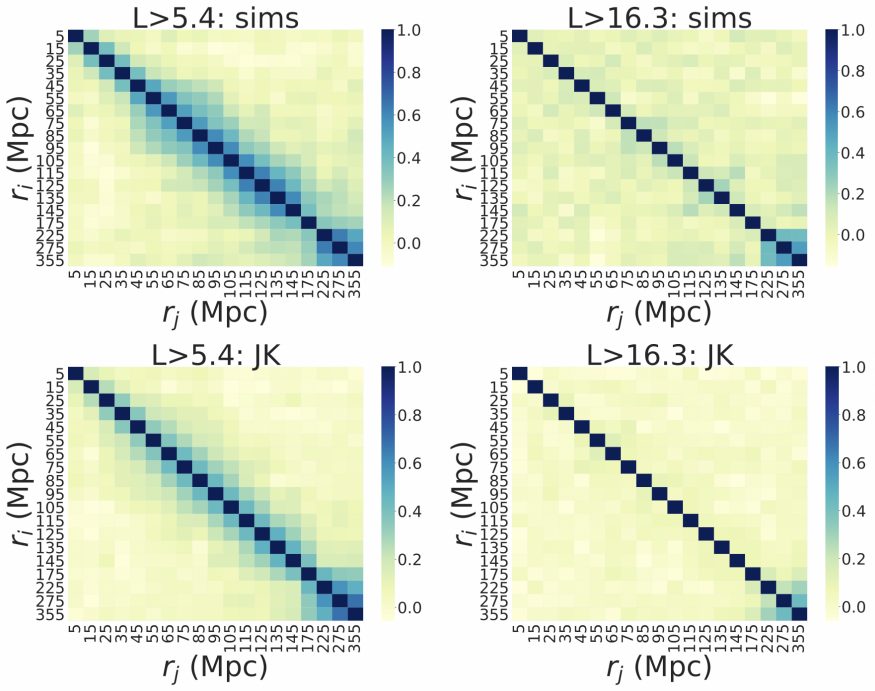

Figure 3.4: Pairwise correlation matrices for the S16 ILC map across the 19 bins in spatial cluster separation, from 5 to 355 Mpc, for two cumulative luminosity bins, $L > 5.4 \times 10^{10} L_{\odot}$[Left] and $> 16.3 \times 10^{10} L_{\odot}$ [Right] derived from simulations [Upper] and the JK [Lower] methods.

a gravitational infall between the cluster pairs, with the mutual gravitational attraction falling off as one moves to cluster pairs separated by larger distances. The magnitude of the signal amplitude increases as the average luminosity of the sample increases, consistent with the observed clusters being more massive haloes with larger optical depths, and with deeper gravitational potentials.

At each luminosity cut, the respective pairs of kSZ signals in Fig. 3.5 and Fig. 3.6, extracted from the two complementary maps show consistency within the 1σ error bars. Given that each has a different approach to removing foreground, their consistency implies the results are robust against significant contamination from frequency dependent foregrounds.

3.4.3 Comparison with theoretical pairwise velocity predictions

We compare the observed pairwise correlations with the linear pairwise velocity correlation predictions for a WMAP9 cosmology using the theoretical forecasting code developed in [53, 54], as described in 3.3.3. Using (3.9) we infer an effective measure of the cluster optical depth, τ, for the observed samples. In our analysis we consider data for galaxy separations 25 Mpc$< r <$395 Mpc. We exclude the lowest two separation bins as at these scales non-linear velocity effects become significant that are not incorporated in the linear theoretical fit. We consistently find the expected trend for τ for the signal as the cumulative luminosity bin magnitude increases - there is a corresponding monotonic decrease in the fit and the errors. We also find an increase in the SNR, due to the increasing sample sizes. The systematic trend is not seen in the disjoint bins. We also see a weaker SNR for the disjoint bins due to the noise from the relatively smaller sample sizes. This is all apparent in Tables 3.2 and 3.3. The cumulative lumi-

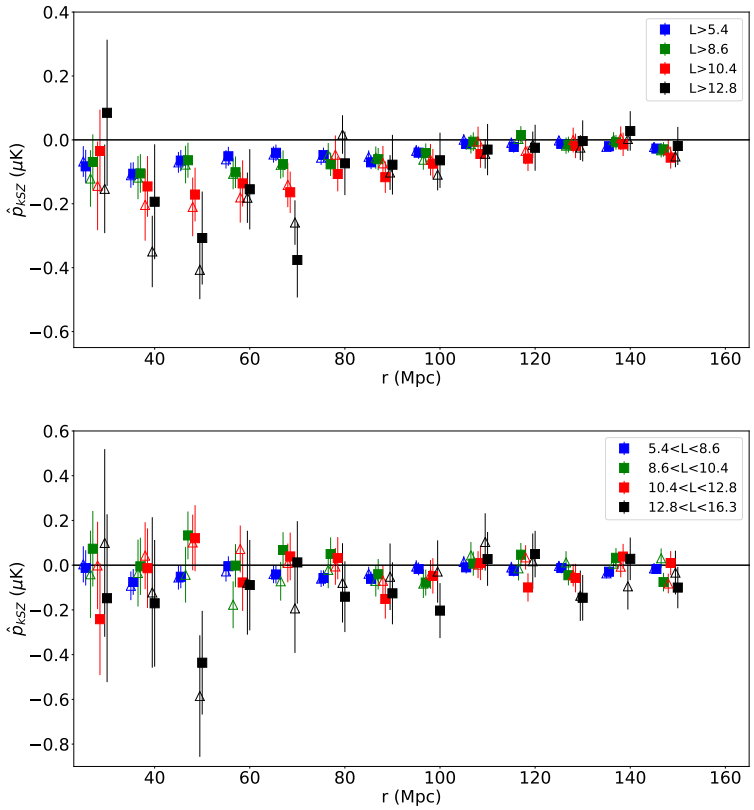

Figure 3.5: Pairwise velocity correlations for the S16 f150 map [empty triangle] and S16 ILC map [full square] for galaxy samples of [upper panel] four cumulative luminosity cuts: L >5.4 [blue], 8.6 [green], 10.4 [red], and 12.8 $\times 10^{10} L_{\odot}$[black] and [lower panel] the four related disjoint luminosity bins.

nosity bins for L >5.4, 9.6, 10.4 and 12.8 $\times 10^{10} L_{\odot}$ each have good agreement with a theoretical pairwise signal that has an SNR > 2.3 for both maps. The disjoint bins, and $L > 16.3 \times 10^{10} L_{\odot}$ bin do not independently yield significant detections of a pairwise signal, each having an SNR< 2.5.

We compare the effect on the τ estimation and the SNR due to simulations, JK, and bootstrap-derived covariance for the S16 ILC map in Table 3.2. We note the highest SNR using the simulations. We find slightly higher PTEs for the JKs and bootstrap methods, especially for the disjoint bins, suggesting that these may be over-estimating

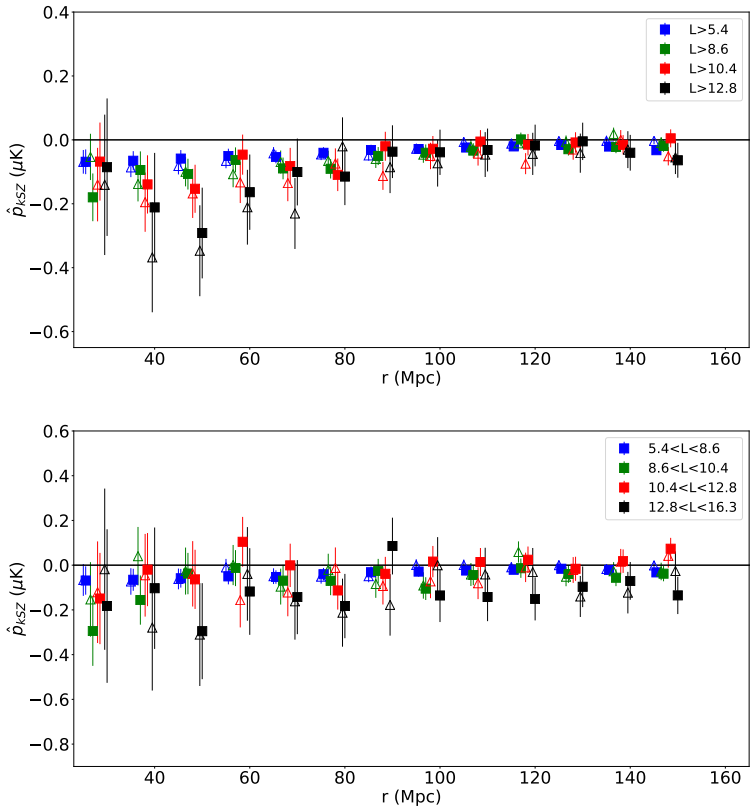

Figure 3.6: As in Figure 3.5 but for the S18 f150 map [empty triangle] and S18 f090 map [full square].

the variance.

In Fig. 3.7 we present the likelihoods for the effective τ value for these three cases. We find overall reasonable consistency in the τ values extracted. We find that the best fit values of τ increase as the minimum luminosity cut threshold increases, congruent with an increase in the the integrated line of sight number density of electrons with cluster mass. Again consistent with the decrease in the sample size, the uncertainty in the τ measurement increases when one considers sequentially higher luminosity thresholds.

In Fig. 3.3, we present the for the three co-added map samples S16 f150 , S18 f150 , and S18 f090 maps using jackknife errors. We find the highest SNR of all of the

Luminosity cut ($\times 10^{10} L_\odot$)	S16 ILC : Sims cov				S16 ILC : JK cov				S16 ILC : Bootstrap cov			
	τ ($\times 10^{-4}$)	χ^2	PTE	SNR	τ ($\times 10^{-4}$)	χ^2	PTE	SNR	τ ($\times 10^{-4}$)	χ^2	PTE	SNR
$L > 5.4$	0.51 ± 0.14	10	0.69	4.1	0.48 ± 0.14	6	0.95	3.4	0.48 ± 0.15	5	0.98	3.3
$L > 8.6$	0.68 ± 0.19	13	0.45	3.7	0.66 ± 0.23	8	0.84	3.3	0.65 ± 0.23	6	0.95	3.1
$L > 10.4$	0.88 ± 0.50	16	0.25	3.7	0.77 ± 0.45	11	0.61	2.9	0.71 ± 0.74	8	0.84	2.4
$L > 12.8$	1.28 ± 0.38	15	0.31	3.3	1.21 ± 0.66	9	0.78	2.7	1.15 ± 0.66	6	0.95	2.3
$L > 16.3$	1.49 ± 1.06	7	0.90	2.3	1.24 ± 1.06	5	0.98	1.4	1.21 ± 1.06	3	0.99	1.2
$5.4 < L < 8.6$	0.50 ± 0.27	6	0.95	1.9	0.54 ± 0.35	3	0.99	1.6	0.53 ± 0.35	3	0.99	1.6
$8.6 < L < 10.4$	-0.026 ± 0.51	15	0.31	0.05	0.02 ± 0.74	10	0.69	0.05	0.11 ± 1.17	6	0.95	0.18
$10.4 < L < 12.8$	0.42 ± 0.69	10	0.69	0.76	0.27 ± 0.95	6	0.95	0.40	0.22 ± 1.06	4	0.99	0.29
$12.8 < L < 16.3$	1.47 ± 0.80	8	0.84	1.8	1.43 ± 1.06	5	0.98	1.4	1.42 ± 1.12	3	0.99	1.3

Table 3.2: A comparison of the best fit τ estimates and 1σ errors for the S16 ILC map for the nine cumulative and disjoint luminosity cuts using the simulation, jackknife and bootstrap estimates of the pairwise correlation covariance matrix. The corresponding χ^2 (for 13 degrees of freedom), SNR and PTE values are also given.

samples, 5.1, for the largest luminosity sample, with the S18 f150 $L > 5.4 \times 10^{10} L_\odot$ cut. The SNR for the preceding ACT analysis [23] was 4.3 for $L > 5.3 \times 10^{10} L_\odot$. We again find that the PTE values suggest the JK errors are overestimated so that we expect the SNR to be a conservative estimate of the signal detection significance. For the S16 f150 and S18 f150 samples we see a trend of increasing τ values in the four cumulative luminosity cuts with the largest SNR. The sample size in the highest luminosity cut is

Luminosity cut ($\times 10^{10} L_\odot$)	S16 f150 : JK cov				S18 f150 : JK cov				S18 f090 : JK cov			
	τ ($\times 10^{-4}$)	χ^2	PTE	SNR	τ ($\times 10^{-4}$)	χ^2	PTE	SNR	τ ($\times 10^{-4}$)	χ^2	PTE	SNR
$L > 5.4$	0.47 ± 0.13	8	0.84	3.9	0.48 ± 0.12	9	0.78	5.1	0.42 ± 0.13	4	0.99	4.3
$L > 8.6$	0.58 ± 0.19	6	0.95	3.4	0.61 ± 0.18	3	0.99	4.4	0.57 ± 0.22	7	0.90	4.1
$L > 10.4$	0.74 ± 0.22	5	0.98	3.4	0.74 ± 0.25	3	0.99	4.1	0.43 ± 0.19	5	0.98	2.2
$L > 12.8$	1.15 ± 0.39	6	0.95	2.9	1.04 ± 0.35	4	0.99	3.2	0.81 ± 0.32	3	0.99	2.6
$L > 16.3$	0.51 ± 0.90	2	0.99	0.68	0.96 ± 1.04	6	0.95	1.5	0.64 ± 0.92	9	0.78	1.0
$5.4 < L < 8.6$	0.51 ± 0.33	5	0.98	1.6	0.49 ± 0.23	6	0.95	2.3	0.38 ± 0.24	13	0.45	1.8
$8.6 < L < 10.4$	0.65 ± 0.65	5	0.98	1.2	0.63 ± 0.43	10	0.69	1.7	0.93 ± 0.61	6	0.95	2.5
$10.4 < L < 12.8$	0.22 ± 0.72	4	0.99	0.33	0.88 ± 0.47	5	0.98	1.9	0.14 ± 0.62	7	0.90	0.30
$12.8 < L < 16.3$	1.34 ± 1.17	5	0.98	1.3	1.61 ± 0.69	5	0.98	2.4	1.72 ± 0.68	6	0.95	2.6

Table 3.3: Best fit τ estimates and 1σ errors for the co-added maps using the S16 observations at 150 GHz [left] and S18 observations at 150 GHz [center] and 90 GHz [right] for the nine cumulative and disjoint luminosity cuts using jackknife estimates of the pairwise correlation covariance matrix. The corresponding χ^2 (for 13 degrees of freedom), SNR and PTE values are also given.

smaller leading to increased uncertainties in the τ value. The S18 f090 τ values do not vary as monotonically. As shown in Fig. 3.7 the likelihoods for the effective τ value for the coadded maps are consistent across the S16 f150 and S18 f150 datasets, with the S18 f090 results consistently a little lower, but still within 1σ.

In Figs. 3.9 and 3.10, we show the cross-correlation measurements for the S16

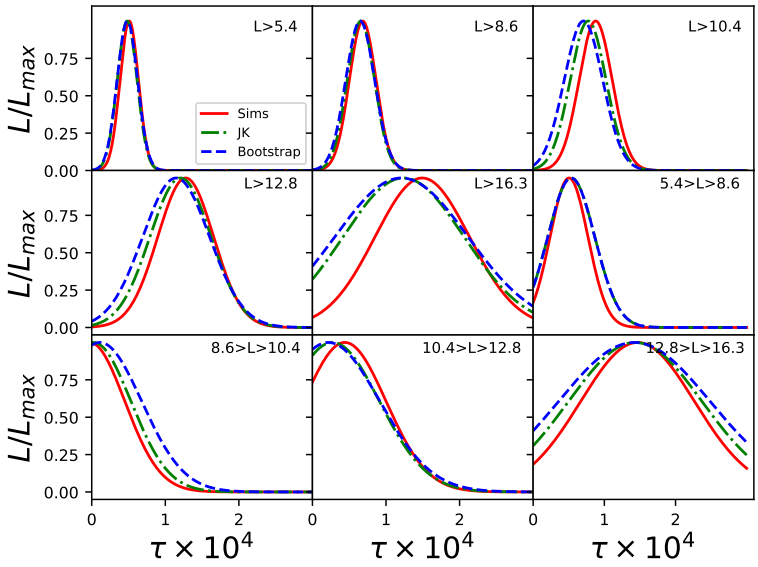

Figure 3.7: The normalized likelihood as a function of τ for the S16 ILC map using the bootstrap [blue dashed], JK [green dashed-dotted] and sims [red full], for each of the nine luminosity cut cluster samples.

ILC maps with the three variance techniques, and S16 f150 , S18 f150 , and S18 f090 maps, respectively with the theoretical model using the best fit and 1σ constraints on τ and the Planck cosmology pairwise velocity predictions. The plots provide an alternative view of the general agreement between the results from the maps. We note that the correlations at higher separations are positive for some of the luminosity cuts, specifically for the S16 ILC and S18 f150 data. As shown in Fig. 3.4 these separation bins are significantly correlated with one another and we find that these data points do not significantly bias or affect the τ constraints.

3.4.4 The impact of cluster miscentering

We have attempted to minimize systematic contamination of the kSZ signal by considering two maps which have foreground mitigation strategies. Another systematic that

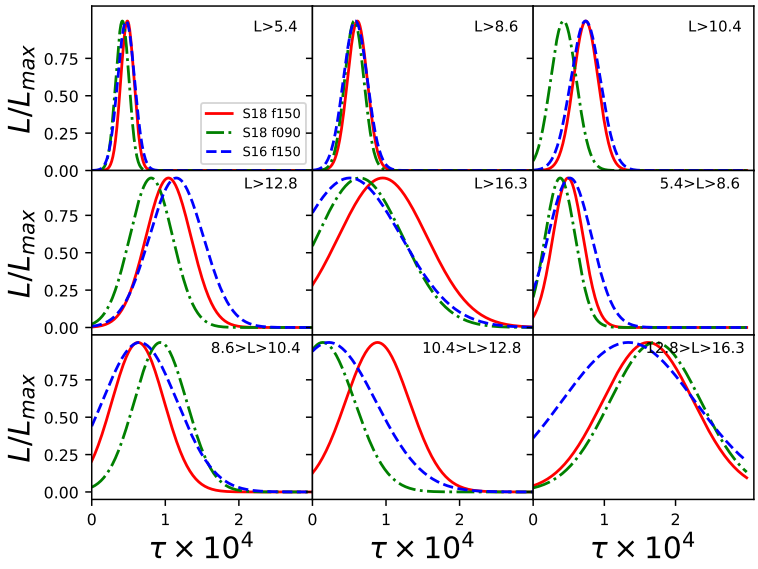

Figure 3.8: The normalized likelihood as a function of τ for the S16 f150 [blue dashed], S18 f150 [red full], and S18 f090 [green dash-dotted] errors for each of the nine luminosity cut cluster samples.

we need to consider will affect both maps in common. This systematic relates to how the galaxy sample is used as a proxy for the cluster location, specifically in identifying the cluster center. In our aperture photometry analysis we are making a well-motivated assumption, known as the 'Central Galaxy Paradigm' [77] that the most massive, most luminous red galaxies in a cluster will reside at the center of the cluster's gravitational potential well. In reality however, the LRGs do not necessarily perfectly trace the cluster center, and can be miscentered and in particular for spectroscopically-selected surveys this can inject additional uncertainties in signal extraction process.

The extent and frequency of miscentering can be characterized by analyzing photometric catalogs which observe many galaxies within a cluster, and determining the distribution of positions of the most luminous galaxies which will be the single or few objects selected in a spectroscopic survey. In two such analyses of the SDSS data red galaxy catalogs, ~20% [39] to ~40% [71] of the most luminous red galaxies where

found to not be tracing the cluster center.

A misidentification of the cluster center, because the proxy galaxy is offset relative to the center, can lead to a misestimation of the aperture photometry temperatures by the disc temperature not including the full cluster signal, and the annulus temperature erroneously containing cluster signal. This can lead to an underestimation of the aperture temperature in (3.3) that then feeds into the average aperture temperature in each redshift bin (3.4) and the resulting estimated kSZ temperatures for all clusters, in (3.2), that are the key ingredients into the pairwise correlator.

To quantify the potential impact of miscentering on our results, we consider an analytic offset model by Johnston et al. [40], obtained through comparing weak lensing profiles with brightest galaxy positions in the SDSS galaxy clusters. It assumes that a fraction of the cluster sample, f_J, has precisely known centers, corresponding to where the brightest galaxy is close to the clusters gravitational potential minimum, and the remaining $(1 - f_J)$ have a brightest galaxy a distance d from the center, with a probability following a Rayleigh distribution function of width σ_J:

$$p_J(d) = \frac{d}{\sigma_J^2} exp\left(-\frac{d^2}{2\sigma_J^2}\right) \tag{3.14}$$

Johnston et al. find a reasonable fit to their BHGs with σ_J=0.42 Mpc/h, and find a richness dependent fraction of BHGs are well-centered, ranging from $f_J \sim 60-90\%$ for clusters of mass 5×10^{12} to $5\times10^{14} M_\odot/h$ respectively. To implement the Johnston offset model we run 50 trials of the pairwise estimator, where each time 25% of the galaxies in the sample are shifted in position by different random a Gaussian of same width σ_J. In our work we use 0.3 and 0.5 Mpc/h, as bounds on the average dispersion of 0.42 Mpc/h.

In Fig. A.1 we present the results of an analysis to estimate the potential impact of the uncertainties in proxy galaxy centering using the randomized off-centering approach for the S18 f150 map and the $L > 5.4\times10^{10} L_\odot$ luminosity bin. We measure the difference

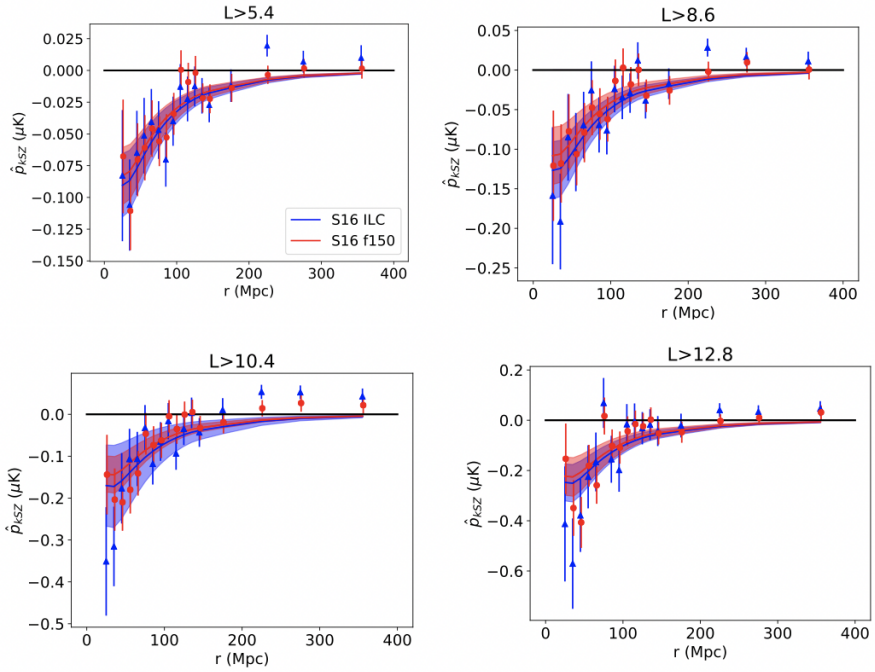

Figure 3.9: From top left to bottom right respectively, the extracted pairwise signal for the S16 ILC [blue triangle] and S16 f150 [red circle] maps for the four cumulative luminosity cuts $L > 5.4, 8.6, 10.4$ and 12.8×10^{10} overlaid with the theoretical pairwise velocity model using the Planck best fit cosmology corresponding to the best fit τ value and 1σ uncertainties given in Tables 3.2 and 3.3.

between the observed signal and that obtained from the 50 random offset resamples,

$$\Delta\hat{p}(r_i) = \hat{p}^{obs}(r_i) - \bar{p}^{offset}(r_i). \tag{3.15}$$

We find that the differences are consistent with zero, indicating that miscentering does not create a systematic bias in the $\hat{p}$ measurement. However we find, consistent with previous work analyzing Planck data [17], that the miscentering creates additional uncertainties in the measurement that could be a notable contribution to the error budget in addition to the jackknife errors.

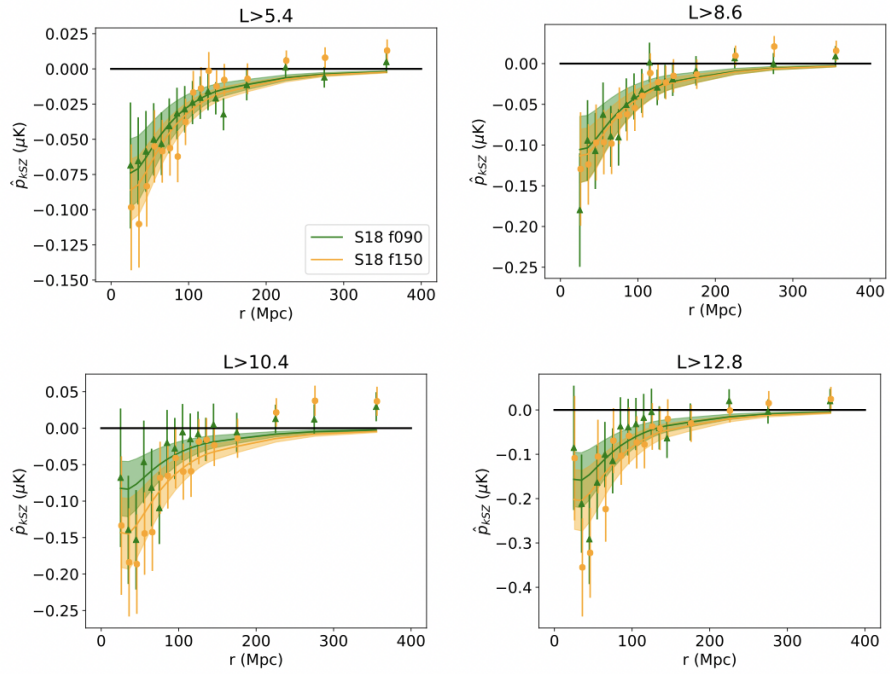

Figure 3.10: As in Fig. 3.9 but for the S18 f150 [orange circle] and S18 f090 [green triangle] maps.

3.5 Conclusions

In this chapter, we present measurements of the optical depth of clusters derived from cross-correlations of pairwise kSZ effect for three co-added maps, S16 f150 , S18 f150 , S18 f090 and one component separated map, S16 ILC , utilizing the most recent ACTPol data combined with Planck. The kSZ signal is obtained by correlating the maps with the BOSS DR15 galaxy catalog using luminous red galaxies as cluster center proxies in five cumulative and four disjoint luminosity cuts with a minimum luminosity threshold of $5.4 \times 10^{10} L_{\odot}$. We obtain a 5.1σ detection using jackknife uncertainties for the $L > 5.4 \times 10^{10} L_{\odot}$ cut containing 342,951 galaxies when crossed with the S18 f150 map with a predicted $\bar{\tau} = (0.48 \pm 0.12) \times 10^{-4}$.

This represents an improvement in SNR relative to that in previous work [23]. The

analysis presented in this chapter includes a comparison of covariance estimates obtained from noise simulation, jackknife and bootstrap methods. We find that noise simulations provide smallest error bars, while the jackknife are the most conservative. Across the methods however, the correlation matrices show significant consistency, with low luminosity cuts resulting in more marked correlations between adjacent cluster separation bins, and the bins at the largest spatial separations having correlations at all frequencies. In this analysis, a number of refinements to the aperture photometry method have been implemented to improve the precision of signal estimation relative to the work in [23]. This includes considering assumptions on pixel size, pixel reprojection, galaxy versus pixel centering of CMB submaps, fractional pixel weighing, and noise-weighting, as outlined in Appendix A.1.

In this multi-frequency analysis, we find consistent results for the component separated map, S16 ILC , and the co-added maps at 98GHz, S18 f090 , and 150GHz S16 f150 and S18 f150 , suggesting a robustness to foreground contamination.

We consider the potential impact of miscentering uncertainties on the kSZ result. By utilizing the Johnston model [40] for brightest galaxy offsets from the cluster center we estimate the impact of this on the kSZ signal. We find that the effect has a relatively small impact jackknife uncertainties being 0.73 greater than miscentering errors at separations of $45 Mpc$. This leads to an associated small increase in the uncertainities of the τ estimate and does not introduce any systematic bias. Our kSZ τ results are compared with tSZ-derived constraints in the companion paper, V20. This analysis paves the way for pairwise kSZ work with this pipeline on upcoming and future data, from additional instruments, for example, Simons Observatory and DESI.

CHAPTER 4

CONCLUSIONS

The kSZ effect, the secondary anisotropy in the CMB due to the peculiar motions of galaxy clusters relative to the CMB rest frame, is a powerful tool for shining a light on the dark sector. A measure of the LSS growth rate, the kSZ effect can provide insights to dark energy and modifications to gravity on a cosmic scale.

The improved resolution and frequency coverage of upcoming CMB instruments and LSS surveys can allow notable improvements in kSZ signal extraction in order to reach these goals. However, astrophysical and analysis systematics must be taken into account. As such, in this thesis we obtain significant pairwise kSZ measurements, while undertaking a careful study of analysis assumptions and the role of systematics such as miscentering.

In Chapter 2, Planck and WMAP CMB data are used in combination with galaxy samples from SDSS, WISE, and DECaLs surveys. Negligible differences in results for the Planck SEVEM and LGMCA maps, for the same galaxy sample, suggesting that the aperture photometry method is robust to the differences in residual foreground removal. This result is highlighted again in Chapter 3 with ACT maps. Also confirmed in Chapter 3 in our more recent ACT analysis, a comparison of flat- vs. noise-weighting CMB maps was found to have little impact on the pairwise statistic from current Planck data. The signal-to-noise ratio was evaluated for the CGC, CMASS+LOWZ and WISE samples. These datasets did not lead to a new significant detection of the kSZ effect, though this is achieved with ACT data in the next chapter.

The impact of miscentering was considered using two complementary techniques: the Johnston analytical offset model and a redMaPPer galaxy selection model. For all

samples, we found that ∼25% of the predicted clusters had brightest galaxies that were offset with a Raleigh distribution with a peak ∼0.3 Mpc/h. In both the direct comparison of BG and CG redMaPPer catalogs and Johnston analytic model, miscentering leads to additional uncertainties equivalent to a significant fraction of the JK error budget. Miscentering was also found to be dominant at the peak of the kSZ signal when compared to photometric redshift errors from DECaLs redMaPPeR, with deviations at the $\sim \sigma$ level. Deviations from photo-z errors of averaged 0.3σ also making them a notable source of error, as in [72] and [45].

Chapter 2 provides quantitative evidence that uncertainties in cluster centering (in terms of both transverse and radial location) can introduce significant uncertainties, comparable to current statistical errors in the kSZ pairwise signal. Order of magnitude improvements in instrumental precision and survey size anticipated with the next generation of CMB and LSS surveys will allow smaller separations, at which the kSZ signal is largest, to be accessible with photometric surveys. Miscentering uncertainties will need to mitigated to fully utilize the incoming data. This work suggests a combination of spectroscopic redshift precision and multiple cluster galaxy populations from photometric surveys, such as will be obtained with Euclid and WFIRST, and in overlapping regions of the DESI and LSST surveys, may be optimal to appropriately constrain both transverse and radial cluster positioning. Similarly this suggests implications for miscentering in kSZ analyses with simulations based on upcoming surveys due to the fact that even the true brightest cluster galaxy does not always trace the location of the projected center of electron distribution.

In Chapter 3, a detection of SNR = 5.1 was obtained using jackknife resampling on the S18 f150 map, an improvement in SNR relative to that in previous work [23]. We additionally present measurements of the optical depth of clusters derived from cross-

correlations of pairwise kSZ effect for three co-added maps, S16 f150 , S18 f150 , S18 f090 and one component separated map, S16 ILC , utilizing the most recent ACTPol data combined with Planck. The kSZ signal is obtained by correlating the maps with the BOSS DR15 galaxy catalog using luminous red galaxies as cluster center proxies in five cumulative and four disjoint luminosity cuts. Optical depth estimates are made for each measurement by comparing with theoretical velocity predictions. We obtain a 5.1σ detection for the largest sample and map area, the $L > 5.4 \times 10^{10} L_{\odot}$ bin on S18 f150 , containing 342,951 galaxies, with a predicted $\bar{\tau} = (0.48 \pm 0.12) \times 10^{-4}$.

The analysis presented in Chapter 3 also includes a comparison of covariance estimates obtained from noise simulation, jackknife and bootstrap methods, in which jackknife errors are found to be the most conservative, while simulations produce the smallest errors. We conduct an analysis on the aperture photometry assumptions, testing pixel size, pixel reprojection, galaxy versus pixel centering of CMB submaps, fractional pixel weighing, and noise-weighting, as outlined in Appendix A.1. This work's results are also contextualized with the previous ACT results [23] in Appendix A.1.

Looking ahead, in the coming decade there will be a wealth of cosmological data, for which the pipeline used in this analysis is ready for use. Future work is planned with Simons Observatory and DESI. This analysis paves the way for pairwise kSZ work with this upcoming and future data.

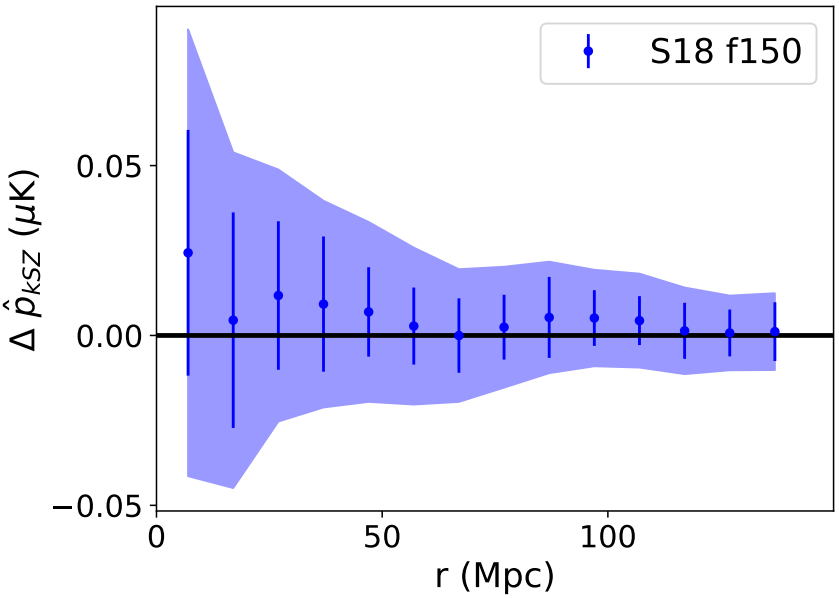

Figure A.1: The uncertainties in signal estimation arising from cluster miscentering, using the Johnston model with Θ=0.42 Mpc/h for the lowest luminosity, $L > 5.4 \times 10^{10} L_{\odot}$ luminosity bin for the S18 f150 [blue] map. The mean and standard error for the difference, $\Delta\hat{p}$, between the observed signal and that of extracted from 50 randomized offset trials is shown by the marker. The shaded regions are the JK errors for the same luminosity cut.

APPENDIX A

A.1 Impact of analysis assumptions on kSZ signal extraction

In this section we present a study of the impact of various differences in analysis assumptions made in this chapter, and the results presented in section 3.4, and the previous ACT kSZ analysis in [23] in which the first three seasons of ACT data [21] and the first season of ACTpol data [55] were cross-correlated with a color-luminosity selected SDSS DR11 galaxy sample.

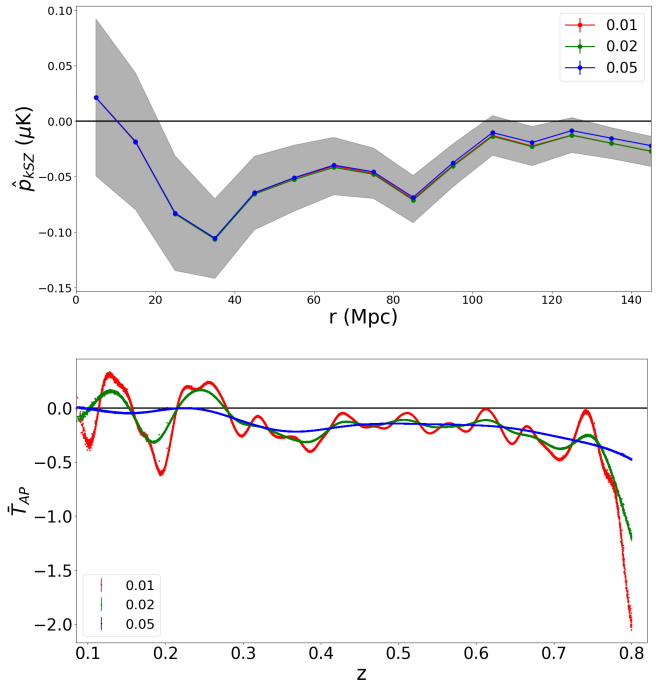

Figure A.2: Comparison of the impact of the redshift smoothing factor in the aperture photometry estimation for the S16 ILC map and the DR15 $L > 5.4 \times 10^{10} L_{\odot}$ galaxy sample. [Upper] The robustness of the $\hat{p}_{kSZ}$ to varying σ_z=0.01, 0.02, 0.05. 1σ uncertainties from sims-based estimates assuming $\sigma = 0.01$ are shown for comparison. [Lower] The individual $\bar{T}_{AP}$ realizations for each case.

We consider five specific differences in the analysis:

- *Pixel size and submap precision:* We use full precision for two pixel parameters that determine which pixels are included in the aperture photometry for a given cluster, that were approximated/rounded in [23]. The "CDELT" parameter determines the pixel size and the second parameter determines which pixel serves as the central pixel for the submap. Rounding errors in these parameters lead to differences in which pixels are identified in the disc/annulus.
- *Reprojection:* We account for the geometrical projection effects, that modify the equal area treatment in aperture photometry when the cluster location is near the

Scenario	ACT map	SDSS sample	Galaxy query & k-correction	CDELT	Submap rounding	Aperture averaging	Submap centering
1	As in [23]	DR11	As in [23]	Approx.	Approx.	Full	Pixel
2	As in [23]	DR11	As in [23]	**Precise**	Approx.	Full	Pixel
3	As in [23]	DR11	As in [23]	Precise	**Precise**	Full	Pixel
4	**S16 f150**	DR11	As in [23]	Precise	Precise	Full	Pixel
5	S16 f150	DR11	As in [23]	Precise	–	**Fractional**	**Galaxy**
6	**S16 ILC**	DR11	As in [23]	Precise	–	Fractional	Galaxy
7	S16 ILC	**DR15**	**V20**	Precise	–	Fractional	Galaxy
8	**S18 f150**	DR15	V20	Precise	–	Fractional	Galaxy

Table A.1: Summary of scenarios utilized in Figure A.3 which demonstrates in a step-by-step fashion the impact of various assumptions used in this analysis and the earlier analysis in [23].

poles rather than the equator, by using the Pixell reprojection subroutine.

- *Pixel vs. galaxy-centered aperture photometry:* Finding the kSZ temperature shift with aperture photometry requires a tracer LRG on which to center the aperture, to determine $\mathbf{r_i}$. In [23], the aperture center was identified as the center of the pixel in which the target galaxy is located. In this analysis, we implement a "galaxy-centered" approach rather than a "pixel-centered" approach in translating the coordinates. This means we determine which temperature values are within the disc and annulus by comparing the equatorial coordinates of the galaxy in catalog with the coordinates on the CMB map. This is opposed to translating the galaxy coordinates to pixel references and populating the disc based on the center of the pixel. As in [23], we us postage stamps rather than full map to speed up the code. Pixell creates reprojected postage stamps recentered on the galaxy location.

- *Fractional pixel weighting:* In implementing the aperture photometry, we account for cases in which pixels are only partially included in the annulus or disc. This includes both pixels centered outside of the disc or ring, and is especially impor-

tant for pixels that span between the disc and annulus. For these pixels, we weight them in the average average based on the fraction of the pixel that overlaps with the aperture according to (3.3).

- *Noise weighting:* We compared flat and noise-weighting schemes for differencing the kSZ temperature decrements in the pairwise momentum estimator in (3.5) and found little difference in the resulting signal.

In Table A.1 and Fig. A.3 we present eight scenarios that allow comparison of the kSZ pairwise results as one transitions from the analysis approach and data used in [23] to that used in our result in systematic, stepwise, fashion. As one can see, comparing scenarios 1 and 8, the key implication for the differences in combination, is a overall reduction in the observed signal amplitude in our analysis relative to that in [23].

Our starting point, scenario 1, utilizes the 2017 map and DR11 sample of 20,000 galaxies and a luminosity cut of $L > 7.9 \times 10^{10} L_{\odot}$ from the analysis in [23]. The end point, scenario 8, uses the S18 f150 map and DR15 sample of 172,409 galaxies used in the analysis in this chapter, after a luminosity cut of $L > 8.6 \times 10^{10} L_{\odot}$.

Scenarios 2 and 3 show that rounding the pixel size and submap centering parameters on the cluster temperatures has a non-negligible effect, reducing the amplitude of the $\hat{p}$ signal extracted for the 20,000 DR11 galaxy sample and 2017 CMB data used in [23]. Using precise values for the parameters decreases the peak amplitude by 27%.

Switching to the S16 f150 used in our chapter, shown in scenario 4, further reduces the amplitude of the signal relative to that in [23] , given in scenario 3. The comparison of scenarios 4 and 5 shows the impact of the transition to the parallelized+Pixell python code used in this chapter, relative to the pipeline used in [23]. For scenario 4 the aperture photometry is centered on the pixel in which the galaxy resides and the cluster

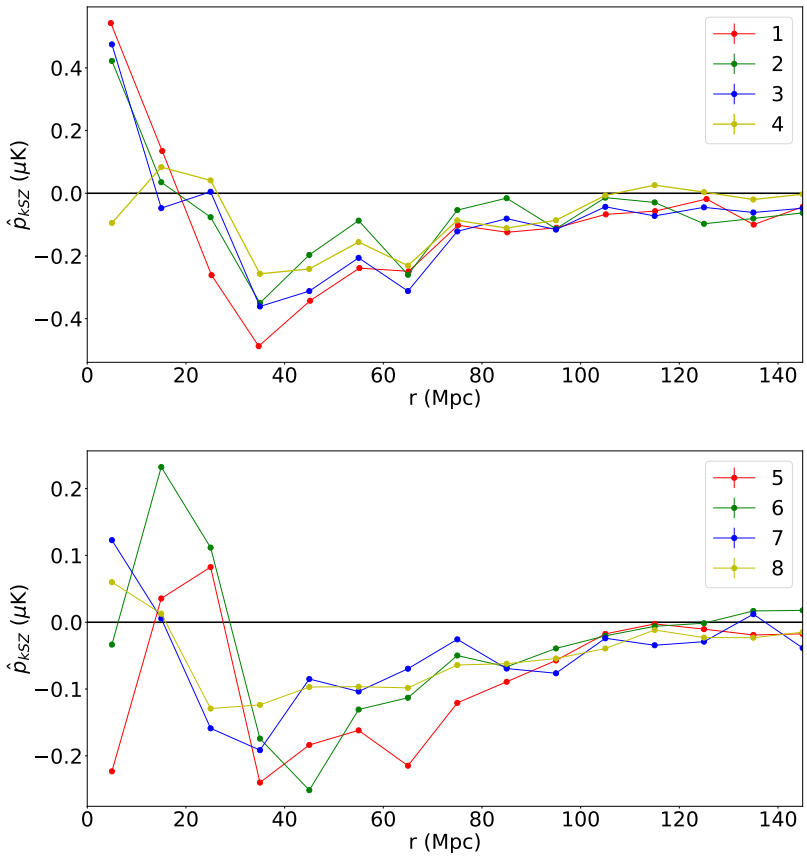

Figure A.3: Comparison of the impact of step-by-step changes in the aperture photometry assumptions in pairwise momentum estimation, $\hat{p}$ obtained from those used in [23] to this work. The stepwise changes in analysis and data are given in Table A.1. [Upper] A comparison of scenarios 1-4 and [Lower] scenarios 5-8. Scenarios 7 and 8 are S16 ILC and S18 f150 results that are analyzed in this chapter.

temperature decrement is obtained by averaging over whole pixels that overlap with the cluster region. By comparison in scenario 5, the aperture photometry is centered on the galaxy location itself and the cluster temperature decrement is obtained by using fractional pixel weighting via bicubic spline interpolation for pixels at the end of the cluster region.

The transition from scenario 5 to scenario 6, shows the difference in signal extraction when using S16 ILC map relative to S16 f150 . The peak amplitude shifts slightly from

around $35Mpc$ to $45Mpc$ while the similar signal amplitude, relative to that in [23] is maintained.

Some differences arising from a difference in the SQL query and k-correction approaches in [23] and our analysis are demonstrated through comparing scenarios 6, using the DR11 query, and scenario 7 which uses our query on the DR15. In scenario 6 we use a sample obtained with a query and k-correct model used in [23], while in scenario 7, we use the SDSS SQL query given in V20, and a publicly available k-correct code [14]. We note that we find differences between the two k-correction approaches, with the luminosities we obtain roughly a factor of 1.24 higher. This results in a shift of the peak amplitude from $45Mpc$ to $35Mpc$.

Finally we compare the newest season of data, S18 f150 , in scenario 8 vs the component separated map, S16 ILC , in 7. We find a slight decrease in the amplitude but a smoother signal overall.

BIBLIOGRAPHY

[1] Kevork N. Abazajian et al. The Seventh Data Release of the Sloan Digital Sky Survey. Astrophys. J. Suppl., 182:543–558, 2009.

[2] Kevork N. Abazajian et al. CMB-S4 Science Book, First Edition. 2016.

[3] P. A. R. Ade et al. Planck 2013 results. XII. Diffuse component separation. Astron. Astrophys., 571:A12, 2014.

[4] P. A. R. Ade et al. Planck 2015 results. XIII. Cosmological parameters. Astron. Astrophys., 594:A13, 2016.

[5] P. A. R. Ade et al. Planck intermediate results. XXXVII. Evidence of unbound gas from the kinetic Sunyaev-Zeldovich effect. Astron. Astrophys., 586:A140, 2016.

[6] D. S. Aguado, Romina Ahumada, Andrés Almeida, Scott F. Anderson, Brett H. Andrews, Borja Anguiano, Erik Aquino Ortíz, Alfonso Aragón-Salamanca, Maria Argudo-Fernández, Marie Aubert, Vladimir Avila-Reese, Carles Badenes, Sand ro Barboza Rembold, Kat Barger, Jorge Barrera-Ballesteros, Dominic Bates, Julian Bautista, Rachael L. Beaton, Timothy C. Beers, Francesco Belfiore, Mariangela Bernardi, Matthew Bershady, Florian Beutler, Jonathan Bird, Dmitry Bizyaev, Guillermo A. Blanc, Michael R. Blanton, Michael Blomqvist, Adam S. Bolton, Médéric Boquien, Jura Borissova, Jo Bovy, William Nielsen Brand t, Jonathan Brinkmann, Joel R. Brownstein, Kevin Bundy, Adam Burgasser, Nell Byler, Mariana Cano Diaz, Michele Cappellari, Ricardo Carrera, Bernardo Cervantes Sodi, Yanping Chen, Brian Cherinka, Peter Doohyun Choi, Haeun Chung, Damien Coffey, Julia M. Comerford, Johan Comparat, Kevin Covey, Gabriele da Silva Ilha, Luiz da Costa, Yu Sophia Dai, Guillermo Damke, Jeremy Darling, Roger Davies, Kyle Dawson, Victoria de Sainte Agathe, Alice Deconto Machado, Agnese Del Moro, Nathan De Lee, Aleksandar M. Diamond-Stanic, Helena Domínguez Sánchez, John Donor, Niv Drory, Hélion du Mas des Bourboux, Chris Duckworth, Tom Dwelly, Garrett Ebelke, Eric Emsellem, Stephanie Escoffier, José G. Fernández-Trincado, Diane Feuillet, Johanna-Laina Fischer, Scott W. Fleming, Amelia Fraser-McKelvie, Gordon Freischlad, Peter M. Frinchaboy, Hai Fu, Lluís Galbany, Rafael Garcia-Dias, D. A. García-Hernández, Luis Alberto Garma Oehmichen, Marcio Antonio Geimba Maia, Héctor Gil-Marín, Kathleen Grabowski, Meng Gu, Hong Guo, Jaewon Ha, Emily Harrington, Sten Hasselquist, Christian R. Hayes, Fred Hearty, Hector Hernandez Toledo, Harry Hicks, David W. Hogg, Kelly Holley-Bockelmann, Jon A. Holtzman, Bau-Ching Hsieh, Jason A. S. Hunt, Ho Seong Hwang, Héctor J. Ibarra-Medel, Camilo Eduardo Jimenez Angel, Jennifer Johnson, Amy Jones, Henrik Jönsson, Karen Kinemuchi, Juna Kollmeier,

Coleman Krawczyk, Kathryn Kreckel, Sandor Kruk, Ivan Lacerna, Ting-Wen Lan, Richard R. Lane, David R. Law, Young-Bae Lee, Cheng Li, Jianhui Lian, Lihwai Lin, Yen-Ting Lin, Chris Lintott, Dan Long, Penélope Longa-Peña, J. Ted Mackereth, Axel de la Macorra, Steven R. Majewski, Olena Malanushenko, Arturo Manchado, Claudia Maraston, Vivek Mariappan, Mariarosa Marinelli, Rui Marques-Chaves, Thomas Masseron, Karen L. Masters, Richard M. McDermid, Nicolás Medina Peña, Sofia Meneses-Goytia, Andrea Merloni, Michael Merrifield, Szabolcs Meszaros, Dante Minniti, Rebecca Minsley, Demitri Muna, Adam D. Myers, Preethi Nair, Janaina Correa do Nascimento, Jeffrey A. Newman, Christian Nitschelm, Matthew D. Olmstead, Audrey Oravetz, Daniel Oravetz, René A. Ortega Minakata, Zach Pace, Nelson Padilla, Pedro A. Palicio, Kaike Pan, Hsi-An Pan, Taniya Parikh, III Parker, James, Sebastien Peirani, Samantha Penny, Will J. Percival, Ismael Perez-Fournon, Thomas Peterken, Marc H. Pinsonneault, Abhishek Prakash, M. Jordan Raddick, Anand Raichoor, Rogemar A. Riffel, Rogério Riffel, Hans-Walter Rix, Annie C. Robin, Alexandre Roman-Lopes, Benjamin Rose, Ashley J. Ross, Graziano Rossi, Kate Rowlands, Kate H. R. Rubin, Sebastián F. Sánchez, José R. Sánchez-Gallego, Conor Sayres, Adam Schaefer, Ricardo P. Schiavon, Jaderson S. Schimoia, Edward Schlafly, David Schlegel, Donald P. Schneider, Mathias Schultheis, Hee-Jong Seo, Shoaib J. Shamsi, Zhengyi Shao, Shiyin Shen, Shravan Shetty, Gregory Simonian, Rebecca J. Smethurst, Jennifer Sobeck, Barbara J. Souter, Ashley Spindler, David V. Stark, Keivan G. Stassun, Matthias Steinmetz, Thaisa Storchi-Bergmann, Guy S. Stringfellow, Genaro Suárez, Jing Sun, Manuchehr Taghizadeh-Popp, Michael S. Talbot, Jamie Tayar, Aniruddha R. Thakar, Daniel Thomas, Patricia Tissera, Rita Tojeiro, Nicholas W. Troup, Eduardo Unda-Sanzana, Octavio Valenzuela, Mariana Vargas-Magaña, José Antonio Vázquez-Mata, David Wake, Benjamin Alan Weaver, Anne-Marie Weijmans, Kyle B. Westfall, Vivienne Wild, John Wilson, Emily Woods, Renbin Yan, Meng Yang, Olga Zamora, Gail Zasowski, Kai Zhang, Zheng Zheng, Zheng Zheng, Guangtun Zhu, Joel C. Zinn, and Hu Zou. The Fifteenth Data Release of the Sloan Digital Sky Surveys: First Release of MaNGA-derived Quantities, Data Visualization Tools, and Stellar Library. Ap. J. S., 240(2):23, Feb 2019.

[7] Christopher P. Ahn et al. The Tenth Data Release of the Sloan Digital Sky Survey: First Spectroscopic Data from the SDSS-III Apache Point Observatory Galactic Evolution Experiment. Astrophys. J. Suppl., 211:17, 2014.

[8] D. Alonso, T. Louis, P. Bull, and P. G. Ferreira. Reconstructing cosmic growth with kSZ observations in the era of Stage IV experiments. ArXiv e-prints, April 2016.

[9] Andrew Arrasmith, Brent Follin, Ethan Anderes, and Lloyd Knox. Tuning Goodness-of-Fit Tests. Mon. Not. Roy. Astron. Soc., 484(2):1889–1898, 2019.

[10] Tobias Baldauf, Vincent Desjacques, and Uro Seljak. Velocity bias in the distribution of dark matter halos. Phys. Rev., D92:123507, 2015.

[11] Nicholas Battaglia. The Tau of Galaxy Clusters. JCAP, 1608(08):058, 2016.

[12] B. A. Benson, S. E. Church, P. A. R. Ade, J. J. Bock, K. M. Ganga, J. R. Hinderks, P. D. Mauskopf, B. Philhour, M. C. Runyan, and K. L. Thompson. Peculiar Velocity Limits from Measurements of the Spectrum of the Sunyaev-Zeldovich Effect in Six Clusters of Galaxies. Ap. J., 592:674–691, August 2003.

[13] M. R. Blanton, J. Brinkmann, I. Csabai, M. Doi, D. Eisenstein, M. Fukugita, J. E. Gunn, D. W. Hogg, and D. J. Schlegel. Estimating Fixed-Frame Galaxy Magnitudes in the Sloan Digital Sky Survey. Astronomical Journal, 125:2348–2360, May 2003.

[14] Michael R. Blanton and Sam Roweis. K-corrections and filter transformations in the ultraviolet, optical, and near infrared. Astron. J., 133:734–754, 2007.

[15] J. Bobin, F. Sureau, J. L. Starck, A. Rassat, and P. Paykari. Joint Planck and WMAP CMB Map Reconstruction. Astron. Astrophys., 563:A105, 2014.

[16] Philip Bull, Timothy Clifton, and Pedro G. Ferreira. The kSZ effect as a test of general radial inhomogeneity in LTB cosmology. Phys. Rev., D85:024002, 2012.

[17] Victoria Calafut, Rachel Bean, and Byeonghee Yu. Cluster mislocation in kinematic Sunyaev-Zeldovich effect extraction. Phys. Rev., D96(12):123529, 2017.

[18] C. E. Cunha, M. Lima, H. Oyaizu, J. Frieman, and H. Lin. Estimating the redshift distribution of photometric galaxy samples - II. Applications and tests of a new method. Mon. Not. R. Astron. Soc., 396:2379–2398, July 2009.

[19] Omar Darwish et al. The Atacama Cosmology Telescope: A CMB lensing mass map over 2100 square degrees of sky and its cross-correlation with BOSS-CMASS galaxies. 4 2020.

[20] S. Das, T. Louis, M. R. Nolta, G. E. Addison, E. S. Battistelli, J. R. Bond, E. Calabrese, D. Crichton, M. J. Devlin, S. Dicker, J. Dunkley, R. Dünner, J. W. Fowler, M. Gralla, A. Hajian, M. Halpern, M. Hasselfield, M. Hilton, A. D. Hincks, R. Hlozek, K. M. Huffenberger, J. P. Hughes, K. D. Irwin, A. Kosowsky, R. H. Lupton, T. A. Marriage, D. Marsden, F. Menanteau, K. Moodley, M. D. Niemack, L. A. Page, B. Partridge, E. D. Reese, B. L. Schmitt, N. Sehgal, B. D. Sherwin, J. L. Sievers, D. N. Spergel, S. T. Staggs, D. S. Swetz, E. R. Switzer, R. Thornton,

H. Trac, and E. Wollack. The Atacama Cosmology Telescope: temperature and gravitational lensing power spectrum measurements from three seasons of data. JCAP, 4:014, April 2014.

[21] Sudeep Das et al. The Atacama Cosmology Telescope: temperature and gravitational lensing power spectrum measurements from three seasons of data. JCAP, 1404:014, 2014.

[22] K. S. Dawson, D. J. Schlegel, C. P. Ahn, S. F. Anderson, É. Aubourg, S. Bailey, R. H. Barkhouser, J. E. Bautista, A. Beifiori, A. A. Berlind, V. Bhardwaj, D. Bizyaev, C. H. Blake, M. R. Blanton, M. Blomqvist, A. S. Bolton, A. Borde, J. Bovy, W. N. Brandt, H. Brewington, J. Brinkmann, P. J. Brown, J. R. Brownstein, K. Bundy, N. G. Busca, W. Carithers, A. R. Carnero, M. A. Carr, Y. Chen, J. Comparat, N. Connolly, F. Cope, R. A. C. Croft, A. J. Cuesta, L. N. da Costa, J. R. A. Davenport, T. Delubac, R. de Putter, S. Dhital, A. Ealet, G. L. Ebelke, D. J. Eisenstein, S. Escoffier, X. Fan, N. Filiz Ak, H. Finley, A. Font-Ribera, R. Génova-Santos, J. E. Gunn, H. Guo, D. Haggard, P. B. Hall, J.-C. Hamilton, B. Harris, D. W. Harris, S. Ho, D. W. Hogg, D. Holder, K. Honscheid, J. Huehnerhoff, B. Jordan, W. P. Jordan, G. Kauffmann, E. A. Kazin, D. Kirkby, M. A. Klaene, J.-P. Kneib, J.-M. Le Goff, K.-G. Lee, D. C. Long, C. P. Loomis, B. Lundgren, R. H. Lupton, M. A. G. Maia, M. Makler, E. Malanushenko, V. Malanushenko, R. Mandelbaum, M. Manera, C. Maraston, D. Margala, K. L. Masters, C. K. McBride, P. McDonald, I. D. McGreer, R. G. McMahon, O. Mena, J. Miralda-Escudé, A. D. Montero-Dorta, F. Montesano, D. Muna, A. D. Myers, T. Naugle, R. C. Nichol, P. Noterdaeme, S. E. Nuza, M. D. Olmstead, A. Oravetz, D. J. Oravetz, R. Owen, N. Padmanabhan, N. Palanque-Delabrouille, K. Pan, J. K. Parejko, I. Pâris, W. J. Percival, I. Pérez-Fournon, I. Pérez-Ràfols, P. Petitjean, R. Pfaffenberger, J. Pforr, M. M. Pieri, F. Prada, A. M. Price-Whelan, M. J. Raddick, R. Rebolo, J. Rich, G. T. Richards, C. M. Rockosi, N. A. Roe, A. J. Ross, N. P. Ross, G. Rossi, J. A. Rubiño-Martin, L. Samushia, A. G. Sánchez, C. Sayres, S. J. Schmidt, D. P. Schneider, C. G. Scóccola, H.-J. Seo, A. Shelden, E. Sheldon, Y. Shen, Y. Shu, A. Slosar, S. A. Smee, S. A. Snedden, F. Stauffer, O. Steele, M. A. Strauss, A. Streblyanska, N. Suzuki, M. E. C. Swanson, T. Tal, M. Tanaka, D. Thomas, J. L. Tinker, R. Tojeiro, C. A. Tremonti, M. Vargas Magaña, L. Verde, M. Viel, D. A. Wake, M. Watson, B. A. Weaver, D. H. Weinberg, B. J. Weiner, A. A. West, M. White, W. M. Wood-Vasey, C. Yeche, I. Zehavi, G.-B. Zhao, and Z. Zheng. The Baryon Oscillation Spectroscopic Survey of SDSS-III. The Astronomical Journal, 145:10, January 2013.

[23] F. De Bernardis et al. Detection of the pairwise kinematic Sunyaev-Zel'dovich effect with BOSS DR11 and the Atacama Cosmology Telescope. JCAP, 1703(03):008, 2017.

[24] S. Ferraro, J. C. Hill, N. Battaglia, J. Liu, and D. N. Spergel. Kinematic Sunyaev-Zel'dovich effect with projected fields. II. Prospects, challenges, and comparison with simulations. Phys. Rev. D, 94(12):123526, December 2016.

[25] P. G. Ferreira, R. Juszkiewicz, H. A. Feldman, M. Davis, and Andrew H. Jaffe. Streaming velocities as a dynamical estimator of omega. Astrophys. J., 515:L1–L4, 1999.

[26] S. Flender, L. Bleem, H. Finkel, S. Habib, K. Heitmann, and G. Holder. Simulations of the Pairwise Kinematic Sunyaev-Zeldovich Signal. ArXiv e-prints, November 2015.

[27] Samuel Flender, Daisuke Nagai, and Michael McDonald. Constraints on the optical depth of galaxy groups and clusters. Astrophys. J., 837(2):124, 2017.

[28] Martin G. Haehnelt and Max Tegmark. Using the kinematic Sunyaev-Zeldovich effect to determine the peculiar velocities of clusters of galaxies. Mon. Not. Roy. Astron. Soc., 279:545–556, 1996.

[29] N. Hand, G. E. Addison, E. Aubourg, N. Battaglia, E. S. Battistelli, D. Bizyaev, J. R. Bond, H. Brewington, J. Brinkmann, B. R. Brown, S. Das, K. S. Dawson, M. J. Devlin, J. Dunkley, R. Dunner, D. J. Eisenstein, J. W. Fowler, M. B. Gralla, A. Hajian, M. Halpern, M. Hilton, A. D. Hincks, R. Hlozek, J. P. Hughes, L. Infante, K. D. Irwin, A. Kosowsky, Y.-T. Lin, E. Malanushenko, V. Malanushenko, T. A. Marriage, D. Marsden, F. Menanteau, K. Moodley, M. D. Niemack, M. R. Nolta, D. Oravetz, L. A. Page, N. Palanque-Delabrouille, K. Pan, E. D. Reese, D. J. Schlegel, D. P. Schneider, N. Sehgal, A. Shelden, J. Sievers, C. Sifón, A. Simmons, S. Snedden, D. N. Spergel, S. T. Staggs, D. S. Swetz, E. R. Switzer, H. Trac, B. A. Weaver, E. J. Wollack, C. Yeche, and C. Zunckel. Evidence of Galaxy Cluster Motions with the Kinematic Sunyaev-Zel'dovich Effect. Physical Review Letters, 109(4):041101, July 2012.

[30] Nick Hand et al. Evidence of Galaxy Cluster Motions with the Kinematic Sunyaev-Zel'dovich Effect. Phys. Rev. Lett., 109:041101, 2012.

[31] J. Hartlap, Patrick Simon, and P. Schneider. Why your model parameter confidences might be too optimistic: Unbiased estimation of the inverse covariance matrix. Astron. Astrophys., 2006. [Astron. Astrophys.464,399(2007)].

[32] C. Hikage, M. Takada, and D. N. Spergel. Using galaxy-galaxy weak lensing measurements to correct the finger of God. Mon. Not. R. Astron. Soc., 419:3457–3481, February 2012.

[33] J. C. Hill, S. Ferraro, N. Battaglia, J. Liu, and D. N. Spergel. The Kinematic Sunyaev-Zel'dovich Effect with Projected Fields: A Novel Probe of the Baryon Distribution with Planck, WMAP, and WISE Data. ArXiv e-prints, March 2016.

[34] J. Colin Hill, Simone Ferraro, Nick Battaglia, Jia Liu, and David N. Spergel. Kinematic Sunyaev-Zel?dovich Effect with Projected Fields: A Novel Probe of the Baryon Distribution with Planck, WMAP, and WISE Data. Phys. Rev. Lett., 117(5):051301, 2016.

[35] J. Colin Hill and David N. Spergel. Detection of thermal SZ-CMB lensing cross-correlation in Planck nominal mission data. JCAP, 1402:030, 2014.

[36] G. Hinshaw, D. Larson, E. Komatsu, D. N. Spergel, C. L. Bennett, J. Dunkley, M. R. Nolta, M. Halpern, R. S. Hill, N. Odegard, L. Page, K. M. Smith, J. L. Weiland, B. Gold, N. Jarosik, A. Kogut, M. Limon, S. S. Meyer, G. S. Tucker, E. Wollack, and E. L. Wright. Nine-year Wilkinson Microwave Anisotropy Probe (WMAP) Observations: Cosmological Parameter Results. Astrophysical Journal Supplement, 208:19, October 2013.

[37] W. L. Holzapfel, P. A. R. Ade, S. E. Church, P. D. Mauskopf, Y. Rephaeli, T. M. Wilbanks, and A. E. Lange. Limits on the Peculiar Velocities of Two Distant Clusters Using the Kinematic Sunyaev-Zeldovich Effect. Ap. J., 481:35–48, May 1997.

[38] H. Hoshino, A. Leauthaud, C. Lackner, C. Hikage, E. Rozo, E. Rykoff, R. Mandelbaum, S. More, A. More, S. Saito, and B. Vulcani. Luminous red galaxies in clusters: central occupation, spatial distributions and miscentring. MNRAS, 452:998–1013, September 2015.

[39] Hanako Hoshino et al. Luminous red galaxies in clusters: central occupation, spatial distributions and miscentring. Mon. Not. Roy. Astron. Soc., 452(1):998–1013, 2015.

[40] David E. Johnston, Erin S. Sheldon, Risa H. Wechsler, Eduardo Rozo, Benjamin P. Koester, Joshua A. Frieman, Timothy A. McKay, August E. Evrard, Matthew R. Becker, and James Annis. Cross-correlation Weak Lensing of SDSS galaxy Clusters II: Cluster Density Profiles and the Mass–Richness Relation. 2007.

[41] A. Kashlinsky and F. Atrio-Barandela. Measuring cosmological bulk flows via the kinematic sunyaev-zeldovich effect in the upcoming cosmic microwave background maps. Astrophys. J., 536:L67, 2000.

[42] A. Kashlinsky, F. Atrio-Barandela, and H. Ebeling. Measuring the dark flow with public X-ray cluster data. Astrophys. J., 732:1, 2011.

[43] A. Kashlinsky, F. Atrio-Barandela, H. Ebeling, A. Edge, and D. Kocevski. A new measurement of the bulk flow of X-ray luminous clusters of galaxies. Astrophys. J., 712:L81–L85, 2010.

[44] R. Keisler. The Statistical Significance of the "Dark Flow". Ap. J. Lett., 707:L42–L44, December 2009.

[45] R. Keisler and F. Schmidt. Prospects for Measuring the Relative Velocities of Galaxy Clusters in Photometric Surveys Using the Kinetic Sunyaev-Zel'dovich Effect. Ap. J. Lett., 765:L32, March 2013.

[46] G. Lavaux, N. Afshordi, and M. J. Hudson. First measurement of the bulk flow of nearby galaxies using the cosmic microwave background. Mon. Not. R. Astron. Soc., 430:1617–1635, April 2013.

[47] Antony Lewis and Sarah Bridle. Cosmological parameters from CMB and other data: A Monte Carlo approach. Physical Review Letters D, 66:103511, 2002.

[48] M. Li, R. E. Angulo, S. D. M. White, and J. Jasche. Matched filter optimization of kSZ measurements with a reconstructed cosmological flow field. MNRAS, 443:2311–2326, September 2014.

[49] Mathew S. Madhavacheril et al. The Atacama Cosmology Telescope: Component-separated maps of CMB temperature and the thermal Sunyaev-Zel'dovich effect. 2019.

[50] Hugo Martel, Fidle Robichaud, and Paramita Barai. Major cluster mergers and the location of the brightest cluster galaxy. The Astrophysical Journal, 786(2):79, 2014.

[51] Avirukt Mittal, Francesco de Bernardis, and Michael D. Niemack. Optimizing measurements of cluster velocities and temperatures for CCAT-prime and future surveys. 2017.

[52] K. Mody and A. Hajian. One Thousand and One Clusters: Measuring the Bulk Flow with the Planck ESZ and X-Ray-selected Galaxy Cluster Catalogs. Ap. J., 758:4, October 2012.

[53] Eva-Maria Mueller, Francesco de Bernardis, Rachel Bean, and Michael D.

Niemack. Constraints on gravity and dark energy from the pairwise kinematic Sunyaev-Zeldovich effect. Astrophys. J., 808(1):47, 2015.

[54] Eva-Maria Mueller, Francesco de Bernardis, Rachel Bean, and Michael D. Niemack. Constraints on massive neutrinos from the pairwise kinematic Sunyaev-Zel?dovich effect. Phys. Rev., D92(6):063501, 2015.

[55] Sigurd Naess et al. The Atacama Cosmology Telescope: CMB Polarization at $200 < \ell < 9000$. JCAP, 1410(10):007, 2014.

[56] M. D. Niemack, P. A. R. Ade, J. Aguirre, F. Barrientos, J. A. Beall, J. R. Bond, J. Britton, H. M. Cho, S. Das, M. J. Devlin, S. Dicker, J. Dunkley, R. Dünner, J. W. Fowler, A. Hajian, M. Halpern, M. Hasselfield, G. C. Hilton, M. Hilton, J. Hubmayr, J. P. Hughes, L. Infante, K. D. Irwin, N. Jarosik, J. Klein, A. Kosowsky, T. A. Marriage, J. McMahon, F. Menanteau, K. Moodley, J. P. Nibarger, M. R. Nolta, L. A. Page, B. Partridge, E. D. Reese, J. Sievers, D. N. Spergel, S. T. Staggs, R. Thornton, C. Tucker, E. Wollack, and K. W. Yoon. ACTPol: a polarization-sensitive receiver for the Atacama Cosmology Telescope. Proceedings of SPIE, 7741:77411S, July 2010.

[57] S. J. Osborne, D. S. Y. Mak, S. E. Church, and E. Pierpaoli. Measuring the Galaxy Cluster Bulk Flow from WMAP Data. Ap. J., 737:98, August 2011.

[58] S. Perlmutter et al. Measurements of Omega and Lambda from 42 high redshift supernovae. Astrophys. J., 517:565–586, 1999.

[59] Planck Collaboration, R. Adam, P. A. R. Ade, N. Aghanim, Y. Akrami, M. I. R. Alves, F. Argüeso, M. Arnaud, F. Arroja, M. Ashdown, and et al. Planck 2015 results. I. Overview of products and scientific results. Astronomy and Astrophysics, 594:A1, September 2016.

[60] Planck Collaboration, P. A. R. Ade, N. Aghanim, M. Arnaud, M. Ashdown, J. Aumont, C. Baccigalupi, A. Balbi, A. J. Banday, R. B. Barreiro, E. Battaner, K. Benabed, A. Benoit-Lévy, J.-P. Bernard, M. Bersanelli, P. Bielewicz, I. Bikmaev, J. Bobin, J. J. Bock, A. Bonaldi, J. R. Bond, J. Borrill, F. R. Bouchet, C. Burigana, R. C. Butler, P. Cabella, J.-F. Cardoso, A. Catalano, A. Chamballu, L.-Y. Chiang, G. Chon, P. R. Christensen, D. L. Clements, S. Colombi, L. P. L. Colombo, B. P. Crill, F. Cuttaia, A. Da Silva, H. Dahle, R. D. Davies, R. J. Davis, P. de Bernardis, G. de Gasperis, G. de Zotti, J. Delabrouille, J. Démoclès, J. M. Diego, K. Dolag, H. Dole, S. Donzelli, O. Doré, U. Dörl, M. Douspis, X. Dupac, T. A. Enßlin, F. Finelli, I. Flores-Cacho, O. Forni, M. Frailis, M. Frommert, S. Galeotta, K. Ganga, R. T. Génova-Santos, M. Giard, G. Giardino, J. Gonzáalez-Nuevo, A. Gregorio, A. Gruppuso, F. K. Hansen, D. Harrison, C. Hernández-Monteagudo,

D. Herranz, S. R. Hildebrandt, E. Hivon, W. A. Holmes, W. Hovest, K. M. Huffenberger, G. Hurier, T. R. Jaffe, A. H. Jaffe, J. Jasche, W. C. Jones, M. Juvela, E. Keihánen, R. Keskitalo, I. Khamitov, T. S. Kisner, J. Knoche, M. Kunz, H. Kurki-Suonio, G. Lagache, A. Lähteenmäki, J.-M. Lamarre, A. Lasenby, C. R. Lawrence, M. Le Jeune, R. Leonardi, P. B. Lilje, M. Linden-Vørnle, M. López-Caniego, J. F. Macías-Pérez, D. Maino, D. S. Y. Mak, N. Mandolesi, M. Maris, F. Marleau, E. Martínez-González, S. Masi, S. Matarrese, P. Mazzotta, A. Melchiorri, J.-B. Melin, L. Mendes, A. Mennella, M. Migliaccio, S. Mitra, M.-A. Miville-Deschênes, A. Moneti, L. Montier, G. Morgante, D. Mortlock, A. Moss, D. Munshi, J. A. Murphy, P. Naselsky, F. Nati, P. Natoli, C. B. Netterfield, H. U. Nørgaard-Nielsen, F. Noviello, D. Novikov, I. Novikov, S. Osborne, L. Pagano, D. Paoletti, O. Perdereau, F. Perrotta, F. Piacentini, M. Piat, E. Pierpaoli, D. Pietrobon, S. Plaszczynski, E. Pointecouteau, G. Polenta, L. Popa, T. Poutanen, G. W. Pratt, S. Prunet, J.-L. Puget, S. Puisieux, J. P. Rachen, R. Rebolo, M. Reinecke, M. Remazeilles, C. Renault, S. Ricciardi, M. Roman, J. A. Rubiño-Martín, B. Rusholme, M. Sandri, G. Savini, D. Scott, L. Spencer, R. Sunyaev, D. Sutton, A.-S. Suur-Uski, J.-F. Sygnet, J. A. Tauber, L. Terenzi, L. Toffolatti, M. Tomasi, M. Tristram, M. Tucci, L. Valenziano, J. Valiviita, B. Van Tent, P. Vielva, F. Villa, N. Vittorio, L. A. Wade, N. Welikala, D. Yvon, A. Zacchei, J. P. Zibin, and A. Zonca. Planck intermediate results. XIII. Constraints on peculiar velocities. Astronomy & Astrophysics, 561:A97, January 2014.

[61] Adam G. Riess et al. Type Ia supernova discoveries at z ¿ 1 from the Hubble Space Telescope: Evidence for past deceleration and constraints on dark energy evolution. Astrophys. J., 607:665–687, 2004.

[62] E. Rozo et al. redMaGiC: Selecting Luminous Red Galaxies from the DES Science Verification Data. Mon. Not. Roy. Astron. Soc., 461(2):1431–1450, 2016.

[63] Eduardo Rozo, Eli S. Rykoff, Matthew Becker, Rachel M. Reddick, and Risa H. Wechsler. redMaPPer ? IV. Photometric membership identification of red cluster galaxies with 1?per?cent precision. Mon. Not. Roy. Astron. Soc., 453(1):38–52, 2015.

[64] E. S. Rykoff et al. redMaPPer I: Algorithm and SDSS DR8 Catalog. Astrophys. J., 785:104, 2014.

[65] E. S. Rykoff et al. The redMaPPer Galaxy Cluster Catalog From DES Science Verification Data. Astrophys. J. Suppl., 224(1):1, 2016.

[66] E. S. Rykoff, B. P. Koester, E. Rozo, J. Annis, A. E. Evrard, S. M. Hansen, J. Hao, D. E. Johnston, T. A. McKay, and R. H. Wechsler. Robust Optical Richness Estimation with Reduced Scatter. Ap. J., 746:178, February 2012.

[67] E. S. Rykoff, E. Rozo, D. Hollowood, A. Bermeo-Hernandez, T. Jeltema, J. Mayers, A. K. Romer, P. Rooney, A. Saro, C. Vergara Cervantes, R. H. Wechsler, H. Wilcox, T. M. C. Abbott, F. B. Abdalla, S. Allam, J. Annis, A. Benoit-Lévy, G. M. Bernstein, E. Bertin, D. Brooks, D. L. Burke, D. Capozzi, A. Carnero Rosell, M. Carrasco Kind, F. J. Castander, M. Childress, C. A. Collins, C. E. Cunha, C. B. D'Andrea, L. N. da Costa, T. M. Davis, S. Desai, H. T. Diehl, J. P. Dietrich, P. Doel, A. E. Evrard, D. A. Finley, B. Flaugher, P. Fosalba, J. Frieman, K. Glazebrook, D. A. Goldstein, D. Gruen, R. A. Gruendl, G. Gutierrez, M. Hilton, K. Honscheid, B. Hoyle, D. J. James, S. T. Kay, K. Kuehn, N. Kuropatkin, O. Lahav, G. F. Lewis, C. Lidman, M. Lima, M. A. G. Maia, R. G. Mann, J. L. Marshall, P. Martini, P. Melchior, C. J. Miller, R. Miquel, J. J. Mohr, R. C. Nichol, B. Nord, R. Ogando, A. A. Plazas, K. Reil, M. Sahlén, E. Sanchez, B. Santiago, V. Scarpine, M. Schubnell, I. Sevilla-Noarbe, R. C. Smith, M. Soares-Santos, F. Sobreira, J. P. Stott, E. Suchyta, M. E. C. Swanson, G. Tarle, D. Thomas, D. Tucker, S. Uddin, P. T. P. Viana, V. Vikram, A. R. Walker, Y. Zhang, and DES Collaboration. The RedMaPPer Galaxy Cluster Catalog From DES Science Verification Data. Ap. J. S., 224:1, May 2016.

[68] A. Saro et al. Constraints on the richness?mass relation and the optical-SZE positional offset distribution for SZE-selected clusters. Mon. Not. Roy. Astron. Soc., 454(3):2305–2319, 2015.

[69] Emmanuel Schaan et al. Evidence for the kinematic Sunyaev-Zel?dovich effect with the Atacama Cosmology Telescope and velocity reconstruction from the Baryon Oscillation Spectroscopic Survey. Phys. Rev., D93(8):082002, 2016.

[70] K. K. Schaffer, T. M. Crawford, K. A. Aird, B. A. Benson, L. E. Bleem, J. E. Carlstrom, C. L. Chang, H. M. Cho, A. T. Crites, T. de Haan, M. A. Dobbs, E. M. George, N. W. Halverson, G. P. Holder, W. L. Holzapfel, S. Hoover, J. D. Hrubes, M. Joy, R. Keisler, L. Knox, A. T. Lee, E. M. Leitch, M. Lueker, D. Luong-Van, J. J. McMahon, J. Mehl, S. S. Meyer, J. J. Mohr, T. E. Montroy, S. Padin, T. Plagge, C. Pryke, C. L. Reichardt, J. E. Ruhl, E. Shirokoff, H. G. Spieler, B. Stalder, Z. Staniszewski, A. A. Stark, K. Story, K. Vanderlinde, J. D. Vieira, and R. Williamson. The first public release of south pole telescope data: Maps of a 95deg2 field from 2008 observations. The Astrophysical Journal, 743(1):90, 2011.

[71] Ramin A. Skibba, Frank C. van den Bosch, Xiaohu Yang, Surhud More, Houjun Mo, and Fabio Fontanot. Are Brightest Halo Galaxies Central Galaxies? Mon. Not. Roy. Astron. Soc., 410:417, 2011.

[72] B. Soergel et al. Detection of the kinematic Sunyaev?Zel'dovich effect with DES Year 1 and SPT. Mon. Not. Roy. Astron. Soc., 461(3):3172–3193, 2016.

[73] B. Soergel, S. Flender, K. T. Story, L. Bleem, T. Giannantonio, G. Efstathiou, E. Rykoff, B. A. Benson, T. Crawford, S. Dodelson, S. Habib, K. Heitmann, G. Holder, B. Jain, E. Rozo, A. Saro, J. Weller, F. B. Abdalla, S. Allam, J. Annis, R. Armstrong, A. Benoit-Lévy, G. M. Bernstein, J. E. Carlstrom, A. Carnero Rosell, M. Carrasco Kind, F. J. Castander, I. Chiu, R. Chown, M. Crocce, C. E. Cunha, C. B. D'Andrea, L. N. da Costa, T. de Haan, S. Desai, H. T. Diehl, J. P. Dietrich, P. Doel, J. Estrada, A. E. Evrard, B. Flaugher, P. Fosalba, J. Frieman, E. Gaztanaga, D. Gruen, R. A. Gruendl, W. L. Holzapfel, K. Honscheid, D. J. James, R. Keisler, K. Kuehn, N. Kuropatkin, O. Lahav, M. Lima, J. L. Marshall, M. McDonald, P. Melchior, C. J. Miller, R. Miquel, B. Nord, R. Ogando, Y. Omori, A. A. Plazas, D. Rapetti, C. L. Reichardt, A. K. Romer, A. Roodman, B. R. Saliwanchik, E. Sanchez, M. Schubnell, I. Sevilla-Noarbe, E. Sheldon, R. C. Smith, M. Soares-Santos, F. Sobreira, A. Stark, E. Suchyta, M. E. C. Swanson, G. Tarle, D. Thomas, J. D. Vieira, A. R. Walker, and N. Whitehorn. Detection of the kinematic Sunyaev-Zel'dovich effect with DES Year 1 and SPT. MNRAS, 461:3172–3193, September 2016.

[74] N. S. Sugiyama, T. Okumura, and D. N. Spergel. Will kinematic Sunyaev-Zel'dovich measurements enhance the science return from galaxy redshift surveys? J. Cosmol. Astropart. Phys., 1:057, January 2017.

[75] R. A. Sunyaev and I. B. Zeldovich. The velocity of clusters of galaxies relative to the microwave background - The possibility of its measurement. MNRAS, 190:413–420, February 1980.

[76] R. A. Sunyaev and Y. B. Zeldovich. Small-Scale Fluctuations of Relic Radiation. Astrophysics and Space Science, 7:3–19, April 1970.

[77] F. C. van den Bosch, S. M. Weinmann, X. Yang, H. J. Mo, C. Li, and Y. P. Jing. The phase-space parameters of the brightest halo galaxies. Mon. Not. R. Astron. Soc., 361:1203–1215, August 2005.

[78] Edward L. Wright, Peter R. M. Eisenhardt, Amy K. Mainzer, Michael E. Ressler, Roc M. Cutri, Thomas Jarrett, J. Davy Kirkpatrick, Deborah Padgett, Robert S. McMillan, Michael Skrutskie, S. A. Stanford, Martin Cohen, Russell G. Walker, John C. Mather, David Leisawitz, III Gautier, Thomas N., Ian McLean, Dominic Benford, Carol J. Lonsdale, Andrew Blain, Bryan Mendez, William R. Irace, Valerie Duval, Fengchuan Liu, Don Royer, Ingolf Heinrichsen, Joan Howard, Mark Shannon, Martha Kendall, Amy L. Walsh, Mark Larsen, Joel G. Cardon, Scott Schick, Mark Schwalm, Mohamed Abid, Beth Fabinsky, Larry Naes, and Chao-Wei Tsai. The Wide-field Infrared Survey Explorer (WISE): Mission Description and Initial On-orbit Performance. Astronomical Journal, 140(6):1868–1881, Dec 2010.

[79] L. Yan, E. Donoso, C.-W. Tsai, D. Stern, R. J. Assef, P. Eisenhardt, A. W. Blain, R. Cutri, T. Jarrett, S. A. Stanford, E. Wright, C. Bridge, and D. A. Riechers. Characterizing the Mid-infrared Extragalactic Sky with WISE and SDSS. Astronomical Journal, 145:55, March 2013.